Available online at www.sciencedirect.com
ScienceDirect
International Journal of Multiphase Flow 34 (2008) 523–546
International Journal of Multiphase Flow
www.elsevier.com/locate/ijmulflow

Review

Quasi-steady shape and drag of deformable bubbles and drops

E. Loth *

Department of Aerospace Engineering, University of Illinois at Urbana-Champaign, Urbana, Illinois, United States

Received 28 November 2006; received in revised form 26 July 2007

Abstract

The quasi-steady shape and drag of isolated drops and bubbles are reviewed in terms of quantitative results, particularly for deformed conditions. Data in the literature were investigated to provide a comprehensive description of observed theoretical, experimental and numerical trends. New descriptions of the aspect ratio and quasi-steady drag coefficient were developed which approach the theoretical limits for creeping flow and attached thin boundary layer conditions, while representing experimental data and resolved-surface simulations at other conditions (many of which are only recently available). These relationships are novel in the sense that they are formulated in terms of the local Weber and Reynolds numbers (as well as density and viscosity ratios), as opposed to static parameters only valid at terminal velocity conditions (e.g. Bond number and Morton numbers). The results indicate that aspect ratio is a unique function of Weber number for fluid particle Reynolds numbers over 100 (especially for clean bubbles and liquid drops in a gas). This is consistent with theoretical results for small deformations. General relations were developed for minimum drag (for a sphere) maximum drag (at maximum-deformation), from which drag increments for intermediate deformation could be defined. These increments correlated especially well with Weber number for clean bubbles and liquid drops in a gas in terms of a group parameter $WeRe_p^{0.2}$. Further research is necessary to integrate these results with effects of neighboring fluid particles and/or walls.

Keywords: Weber number; Reynolds number; Aspect ratio; Spheroid

1. Spherical solid particles

With respect to the velocities of the different phases, the particle velocity ($\mathbf{v}$) is defined as the translational velocity of the particle center of mass ($\mathbf{x}_p$). The continuous-fluid velocity ($\mathbf{u}$) is generally defined in all areas of the domain unoccupied by particles. However, a hypothetical continuous-phase velocity can be extrapolated to the particle centroid as $\mathbf{u}$ and termed the "unhindered velocity". The relative velocity of the particles ($\mathbf{w}$) is then based on the unhindered velocity, i.e. along a particle trajectory

$$\mathbf{w}(t) \equiv \mathbf{v}(t) - \mathbf{u}(t) \tag{1}$$

It is important to note that $\mathbf{u}_{@p}$ does *not* include the fluid dynamic effects resulting from the presence of the particle itself. Assuming that the particle and the far-field velocities are steady and the flow is spatially uniform, the dependence of drag on the magnitude of the relative velocity is primarily dictated by the particle Reynolds number (Re_p), defined as

$$Re_p \equiv \frac{\rho_f |w| d}{\mu_f} \tag{2}$$

In this expression d is the particle diameter, ρ_f is the continuous-phase density, and μ_f is the continuous-phase viscosity. The low Reynolds number condition is often called the "creeping flow" condition and leads to a fully attached laminar flow over the particle and drag as

$$\mathbf{F}_D = -3\pi d \mu_f \mathbf{w} \tag{3}$$

This is often referred to as the Stokes regime owing to his 1851 derivation.

At high Reynolds numbers given by $2000 < Re_p < 300{,}000$, a laminar boundary layer will form on the front of the particle ($\theta = 0°$) and will separate at $\theta \sim 80°$

* Address: 306, Talbot Laboratory, 104 South Wright Street Urbana, IL 61801-2935, United States. Tel.: +1 217 244 5581.
E-mail address: loth@uiuc.edu

0301-9322/$ - see front matter © 2007 Elsevier Ltd. All rights reserved.
doi:10.1016/j.ijmultiphaseflow.2007.08.010

producing a fully turbulent wake behind the particle. The drag coefficient (C_D) written in terms of the total drag force is

$$\mathbf{F}_D \equiv -\frac{\pi}{8} d^2 \rho_f C_D w \mathbf{w} \tag{4}$$

Measurements in the range have shown that C_D is approximately constant in this Re_p range. This nearly constant value is called the "critical drag coefficient" ($C_{D,crit}$) with a value of about 0.4 to 0.45. This Re_p range is often called the "Newton regime", owing to his assumption of a constant drag coefficient for ballistics. One may quantify the departure of the drag from the Stokes solution due to Reynolds number with the Stokes correction factor

$$f_{Re} \equiv \frac{F_D(Re_p)}{F_D(Re_p \to 0)} = \frac{C_D(Re_p)}{24/Re_p} \tag{5}$$

For a solid particle, this ratio is unity for Re_p "1 and is proportional to Re_p for the Newton regime (ca. $3000 < Re_p < 200{,}000$). Higher Reynolds numbers correspond to the supercritical regime, but particles are rarely at such conditions.

For intermediate particle Reynolds numbers (ca. $0.1 < Re_p < 2000$), the flow behind the particle changes from an attached laminar wake, to a separated laminar wake, to an unsteady transitional and then turbulent wake. Since there is no general analytical solution for intermediate Reynolds numbers, the intermediate conditions are generally prescribed by an empirical expression of the drag coefficient. A common and reasonably accurate single sub-critical expression (to within 6% error of the experimental data) for $Re_p < 2 \times 10^5$ is given by Clift and Gauvin (1970) as

$$C_D = \left[\frac{24}{Re_p}\left(1 + 0.15 Re_p^{0.687}\right)\right] + \frac{0.42}{1 + \frac{42{,}500}{Re_p^{1.16}}} \tag{6}$$

The term in square brackets is the commonly known Schiller-Naumann (1933) drag which is quite accurate for $Re_p < 800$, and can be written in terms of the Stokes correction as

$$f_{Re} = 1 + 0.15 Re_p^{0.687} \tag{7}$$

Note that the drag given by Eqs. (6) and (7) represents the time-averaged component for $Re_p > 200$, since some force unsteadiness results from the unsteady separated wake region. It should be noted that the above results are for an isolated particle with one-way coupling, which is focus of this study. However, the presence of finite concentrations of particles will generally yield significant changes. This can include two-way coupling (where particles affect the fluid), three-way coupling (where particles affect each other through fluid dynamics such as drafting), and four-way coupling (where particle–particle collisions can be important). Generally, void fractions and mass fractions of 0.1% or even less are needed to ensure one-way coupling alone is reasonable (Elghobashi, 1994).

2. Spherical fluid particles

If the instantaneous Weber number is sufficiently low, fluid particles are generally spherical in shape. Therefore, the drag is dependent primarily on the surface conditions arising from the influence of viscosity ratio ($\mu = \mu_p/\mu_f$), density ratio ($\rho = \rho_p/\rho_f$), and surfactants. If the particle is fully-contaminated, its surface can be considered as a no-slip condition. In this case, the expressions for a solid particle are appropriate. However, if the particle is pure, there is a slip flow along the particle interface which is driven by internal circulation and the Stokes correction for internal circulation follows the Hadamard–Rybczynski result

$$f_{\mu^*} \equiv \frac{F_D(\mu^*, Re_p \to 0)}{3\pi d \mu_f w} = \frac{2 + 3\mu^*}{3 + 3\mu^*} \tag{8}$$

The purity assumption used above for the Hadamard–Rybczynski solution indicates that the interface is free of any surface-active contaminants (surfactants). However, water interfaces are extremely susceptible to contaminants especially at small diameters. Herein, we will only consider clean (or nearly so) and fully-contaminated conditions.

As the Stokes solid-particle drag solution was extended to include linearized inertial terms by the Oseen expression, Brenner and Cox (1963) extended the Hadamard–Rybczynski expression to include inertial terms for a spherical fluid particle. This yields small but finite Re_p correction terms:

$$f_{\mu^*} = \frac{2 + 3\mu^*}{3 + 3\mu^*} + \frac{3}{16} Re_p \left(\frac{2 + 3\mu^*}{3 + 3\mu^*}\right)^2 + O\left(Re_p^2 \ln Re_p\right) \tag{9}$$

As μ^* approaches ∞, this expression approaches the Oseen expression, and in the limit of μ^* approaching zero (e.g. gas bubble in a liquid), the linearized drag coefficient approaches $C_D = 16/Re_p + 2$. The linearized expression is reasonable up until about Re_p of unity (as was found for the Oseen correction).

When the Reynolds number becomes greater than unity, the above expressions are no longer applicable. As with the solid-sphere case, the fluid physics change substantially for large Reynolds numbers, but are also sensitive to μ^*. As discussed by Clift et al. (1978), flow separation for a spherical droplet in a gas at $\mu^* = 55$ or a fully-contaminated bubble is similar to that of a solid particle since the surface condition is effectively a no-slip condition. As such, the drag for both closely mimics that for a solid-sphere, e.g. to within 1–2%, so that the empirical Schiller-Naumann expression (Eq. (7)) is appropriate up to Re_p of 1000 so long as there is negligible deformation.

In contrast, a spherical gas bubble in a liquid at $\mu^* = 0$ with an uncontaminated interface will have internal recirculation which eliminates any wake separation of the external liquid, at *all Reynolds numbers*. The lack of separation fortunately allows closed-form theoretical solutions. In particular, Levich (1949, 1962) obtained an estimate in

the limit of high Reynolds numbers ($C_D = 48/\ Re_p$) based on the balance of work done by drag and the viscous dissipation in the interior. Moore (1963) extended the theory to intermediate Reynolds numbers by assuming a thin boundary layer on the surface yielding

$$f_{Re\gg 1,\mu^*\to 0} = 2\left[1 - \frac{2.21}{\sqrt{Re}_p}\right] + O\left(Re_p^{-11/6}\right) \tag{10}$$

The term in the square brackets represents Moore's correction to the Levich drag, and this expression was found to be quite reasonable for Re_p as low as 100. To bridge the gap between the Moore and Hadamard–Rybczynski theoretical results, Mei et al. (1994) proposed the following empirical blended function which tends properly to each limit

$$f_{Re,\mu^*\to 0} = \frac{2}{3}\left\{1 + \left[\frac{8}{Re_p} + \frac{1}{2}\left(1 + \frac{3.315}{\sqrt{Re_p}}\right)\right]^{-1}\right\} \tag{11}$$

For a wide range of Reynolds numbers, this expression shows good comparison with both clean bubble experimental data (Fig. 1) and resolved-surface simulations (Takagi and Matsumoto, 1999; Magnaudet and Eames, 2000).

Since flow separation may occur for intermediate values of μ^*, analytical solutions are not available at high Reynolds numbers. Therefore, guidance can be taken from experiments and resolved-surface simulations of Fig. 1. As with the Hadamard–Rybczynski result, particle drag was found to monotonically decrease as the viscosity ratio is reduced. The increment in drag for a clean fluid particle beyond that of a clean bubble can be normalized by the difference between the solid-sphere and clean bubble results. This ratio is defined as Δf^* which varies from zero to unity as the particle viscosity ratio increases and can be modeled in terms of the combined effects of μ^* and Re_p as follows:

$$\begin{aligned}\Delta f^* &\equiv \frac{f_{Re,\mu^*} - f_{Re,\mu^*\to 0}}{f_{Re,\mu^*\to\infty} - f_{Re,\mu^*\to 0}} \\ &= \frac{m + 0.01Re_p(0.4\ \mathrm{m} - 0.8\ \mathrm{m}^2 + 1.4\mathrm{m}^3)}{1 + 0.01Re_p}\end{aligned} \tag{12}$$

The RHS is an empirical expression uses a viscosity ratio function $m \equiv \mu^*/(1+\mu^*)$ and is based on the available data. As shown in Fig. 1, this expression combined with Eqs. (7) and (11) gives reasonable predictions at least until a Re_p of about 1000, beyond which fluid particles tend to deform. Similar correlations for the viscosity ratio effect are given by Clift et al. (1978) and Feng and Michealidis (2001), which also involve multiple equations. This expression combined with Eqs. (7) and (11) is yields reasonable predictions at least for $Re_p < 1000$. At higher Reynolds numbers, there is no quantitative data available for spherical fluid particles with intermediate viscosities (e.g. immiscible drops in a liquid) since they are generally deformed.

Before addressing the non-spherical fluid particle drag, we address the effects of contamination at intermediate Reynolds numbers for spherical particles. The contaminant influence is a function of the surfactant properties and their concentration as well as the chemical composition of both the continuous-phase and dispersed-phase liquid properties. The effect of the surfactant concentration on the fluid particle interface can be broadly classified into three regimes: pure, partially-contaminated, and fully-contaminated. The "pure" condition allows a fully mobile interface with full internal recirculation and corresponds to $\theta_{clean} = 180°$, where θ_{clean} is the angle from the leading edge over which the interface is free of contaminants. As the concentration on the surface increases, parts of the fluid particle surface become immobile and the recirculation is limited to a fraction of the surface ($0° < \theta_{clean} < 180°$). This "partially-contaminated" condition is generally associated with an increased drag (e.g. reduced terminal velocity). As the surfactant concentration increases further, the surface of the fluid particle eventually saturates with surfactants representing a "fully-contaminated" condition corresponding to $\theta_{clean} = 0°$. At this point the surface conditions and terminal velocity of the fluid particle resemble that of a solid body of the same dimension and are approximately independent of further concentration increases.

Roughly, concentration levels below 10^{-7} g/l can be considered pure for most fluid particles, while concentrations above 10^{-2} g/l can be considered fully-contaminated. Water is especially susceptible to the influence of surfactants, making it difficult to achieve pure conditions, especially for small particle diameters. The surfactant properties of importance include solubility, surface pressure, cation and organic concentration, molecular weight, etc. so that generalizations are difficult. For example, water with a surfactant concentration of 10^{-3} g/l can be considered as pure for a 1.55 mm bubble if the surfactant is Sodium dodecyl sulfate, whereas the same bubble in the Triton X-100 solution will be considered fully-contaminated. Water itself is often classified as tap water, distilled water or hyper-clean water. Distilled water is obtained by heating water to form vapor, leaving behind impurities which have higher boiling points then water. However, many organic substances are easily dissolved in water and have similar or lower boiling point then water, making them notoriously difficult to remove. In order to obtain further purify water, various filtration systems (deionization, reverse osmosis, etc.) and UV light are employed to extrude surfactants. Even with these techniques, a pure condition can only be expected for bubbles of diameters greater then 0.7 mm for hyper-clean water. As a result, few, if any, researchers have obtained pure conditions for bubbles with diameters less than 50 μm in water solutions.

For fully-contaminated conditions, the fluid particle will have a negligible value of θ_{clean} and so will follow the rigid sphere drag coefficient curve due to immobilization of the interface. Similarly, pure conditions will yield drag coefficients corresponding to Eq. (12). For partially-contami-

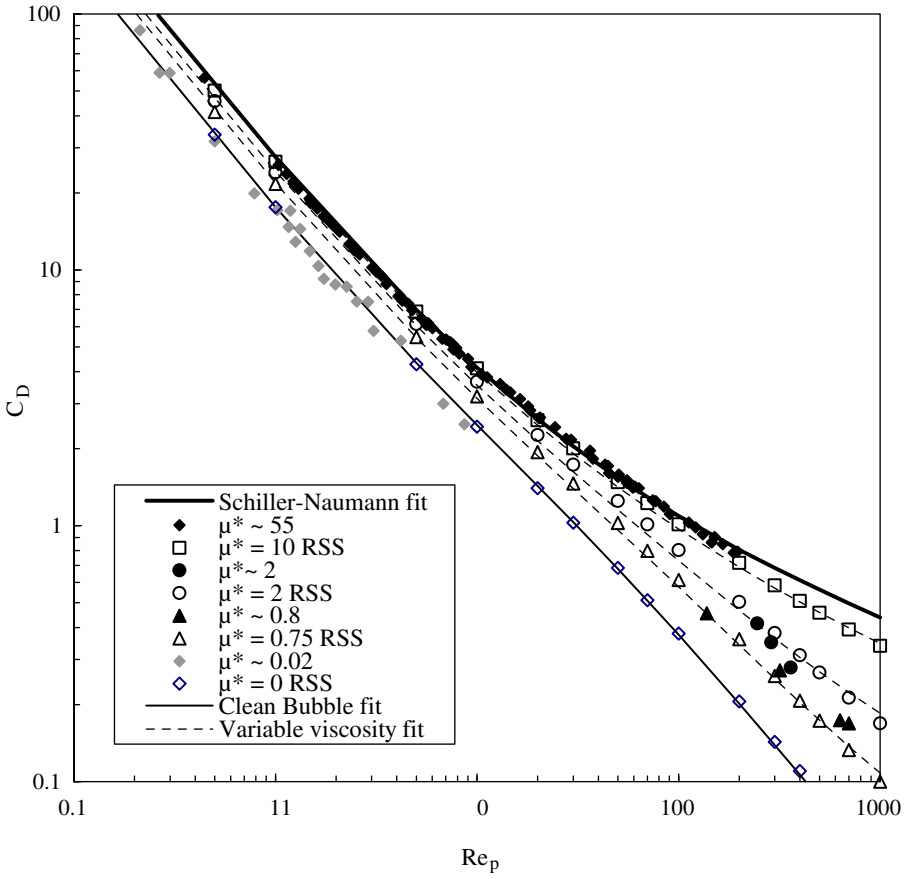

Fig. 1. Drag coefficient for various viscosity ratios from experiments of drops in gas (Beard and Prupacher, 1969), clean bubbles (Haberman and Morton, 1953; Miyahara and Takahashi, 1985) and intermediate viscosity drops in liquids (Winnikow and Chao, 1966). Also shown are resolved-surface simulations of Feng and Michealidis (2001) as well as variable viscosity fits for $\mu^* = 0$ (clean bubble), 0.75, 2, 10, and ∞ (solid-sphere).

nated conditions, no analytical solutions are available. However, Magnaudet and Eames (2000) noted that the theoretical variation can be at least qualitatively extended to higher Reynolds numbers (based on resolved-surface simulations) by assuming the same functional dependence on the clean bubble angle but using the intermediate Reynolds number corrections for the clean and contaminated limits. If we write this relationship for the more general variable viscosity case it becomes:

$$\frac{f_{Re_p,\theta_{clean},\mu^*} - f_{Re_p,\mu^*}}{f_{Re_p,\mu^*\to\infty} - f_{Re_p,\mu^*}} = \frac{2\pi - 2\theta_{clean} + \sin\theta_{clean} + \sin 2\theta_{clean} - \frac{1}{3}\sin 3\theta_{clean}}{2\pi} \tag{13}$$

The limits on the LHS ($f_{Re_p,\mu^*\to\infty}, f_{Re_p,\mu^*}$) can be obtained from Eqs. (7) and (11) so that knowledge of θ_{clean} would allow computation of the drag correction. While it is generally difficult to relate θ_{clean} to surfactant concentration, particle and continuous-phase properties, and time of residence, the expressions of Bel Fdhila and Duineveld (1996) show reasonable agreement with their experimental results.

3. Deformed fluid particle shapes and parameters

Dispersed fluid particles (bubbles and drops away from walls) can deform based on the interplay of surface tension and the fluid-dynamic stresses on the particle surface. Thus, the shape of a fluid particle is not permanent and deforms according to the local stresses imparted by the surrounding environment. The surface tension forces will always drive a free particle toward a spherical shape, whereas initial conditions and/or fluid-dynamic forces are the primary sources of non-sphericity. Fluid particle shapes which are mild deviations from the spherical case are generally a spheroid. The aspect ratio of spheroids can be defined as the ratio of the diameter along the axis of symmetry to the diameter about the axis of symmetry, i.e. $E = d_\parallel/d_\perp$. Most spheroidal fluid particles are oblate ($E < 1$). This ellipsoidal shape reasonably describes the initial deformations that occur for air bubbles in water and water drops in air at terminal conditions (Fig. 2).

3.1. Relationship between Weber number and shape

The importance of the fluid surface stresses on particle deformation tends to scale with the dynamic pressure seen

by the particle since it is the surface pressure distribution and surface tension which control the deformation. This pressure distribution, in turn, can be characterized by the viscosity ratio (which controls recirculation) and the Reynolds number (which controls importance of viscosity). However, the deformation is also related to the surface tension and is thus influenced by the Weber number, which is the ratio of continuous-fluid stresses (which cause deformation) to surface tension stresses (which resist deformation):

$$We = \frac{\rho_f w^2 d}{\sigma} \tag{14}$$

where σ is the surface tension between the particle fluid and that of the surrounding fluid.

The influence of these various parameters on both shape and drag has been investigated theoretically by many researchers with perhaps the most important results given by Saito (1913), Taylor and Acrivos (1964), and Moore (1965). Saito examined the creeping flow limit of $Re_p \ll 1$ (where inertial terms are neglected), and showed that a fluid particle of any viscosity ratio and Weber number will remain spherical. This criterion can be qualitatively expressed as

$$Re_p \ll 1 \quad \text{particles rapidly tend to spherical geometry} \tag{15}$$

To quantify this relationship, one may suggest that fluid particles are spherical for $Re_p < 0.1$. Experimentally observed shapes at such Reynolds numbers are at least qualitatively consistent with this result. For example, the data of Pan and Acrivos (1968), Grace (1973), Grace et al. (1976), and Bhaga and Weber (1981) suggest approximate criteria of $Re_p < 0.2$ for clean bubbles and $Re_p < 0.5$ for contaminated bubbles and drops (Fig. 3).

Taylor and Acrivos extended this condition to small but finite Re_p values by retaining but linearizing the convection terms. For this condition, they noted that deformation is principally controlled by Weber number, and that theoretical onset of ellipsoidal condition ($E \leqslant 0.9$) occurs at $We = 0.64$ for clean bubbles. At very high Reynolds numbers, Moore analyzed gas bubbles and found that onset of ellipsoidal shapes occurs at $We = 0.79$. These results are also consistent with experiments, which also showed that very large Weber numbers coincide with highly-deformed bubbles and drops. In summary, the degree of deformation at finite Re_p can be qualitatively expressed as

$$\begin{aligned} We &\ll 1 \quad \text{particles rapidly tend to spherical geometry} \\ We &\sim 1 \quad \text{moderate deviations from a sphere can occur} \\ We &\gg 1 \quad \text{large deviations from a sphere can occur} \end{aligned} \tag{16}$$

These trends are consistent with measurements for a wide range of Reynolds numbers (from 1 to 10,000) based on the above cited data and those to be presented herein. The general shape transition for these conditions at terminal velocity is shown in Fig. 4 for the case of buoyant bubbles and drops in a liquid (also see Figs. 2 and 3). In all cases, the weakly deformed condition corresponds to an oblate spheroid.

For bubbles ($\rho^* \ll 1$ and $\mu^* \ll 1$), an increase in We_{term} will lead to a flatter aft portion (bottom) as shown in Fig. 4. This is due to a combination of buoyancy and flow recirculation effects which tend to yield a uniform pressure separation region that causes the rear interface to become nearly horizontal when surface tension is weak. For $Re_{p,term} > 100$, large deformations lead to a "spherical-cap" bubble with a hemi-spherical shape on the top and

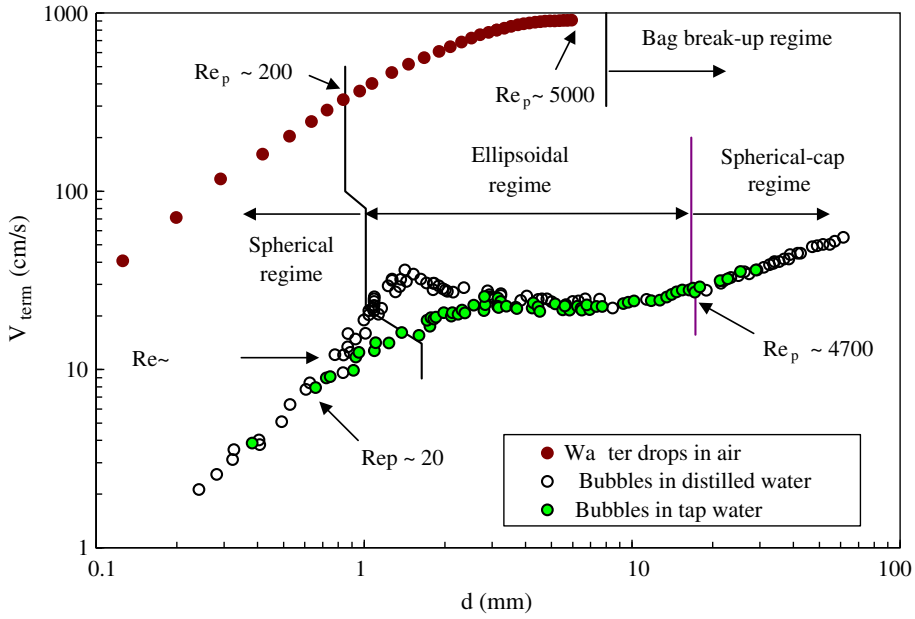

Fig. 2. Terminal velocities of water drops in air from Beard (1976) and air bubbles in water from Haberman and Morton (1954), and Clift et al. (1978).

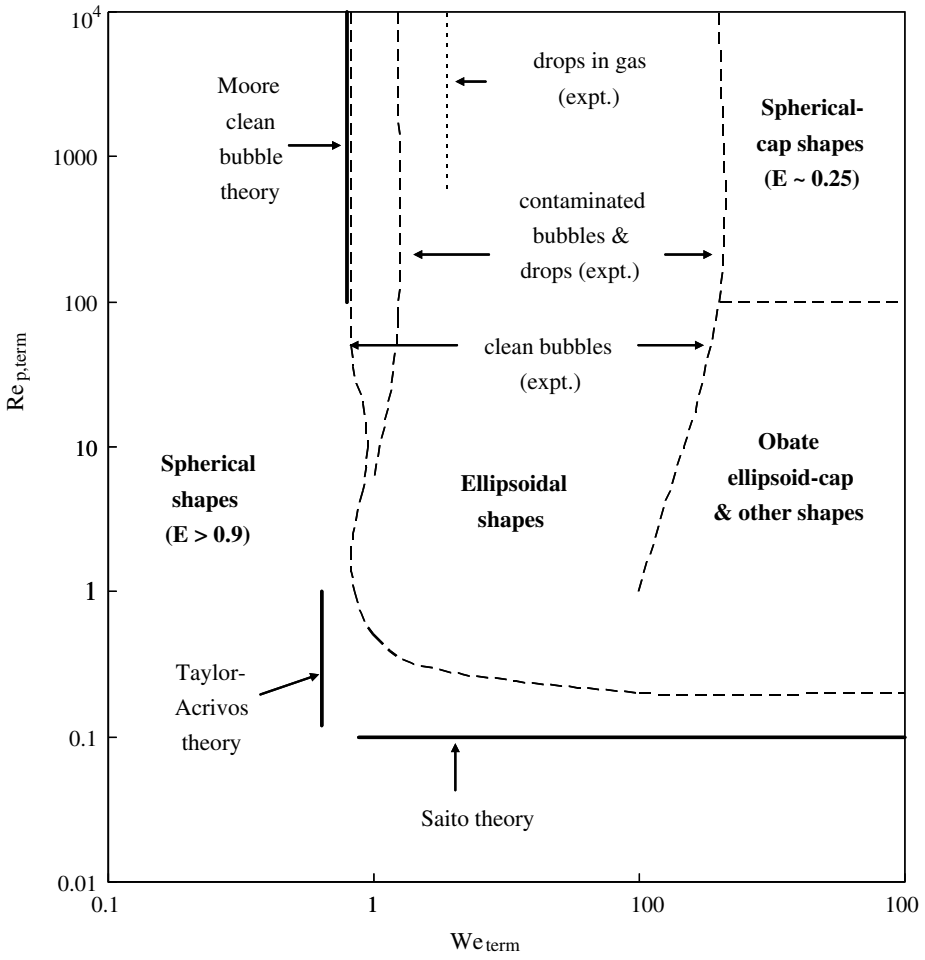

Fig. 3. Qualitative boundaries for terminal shapes for bubbles and drops based on data presented in the following figures for ellipsoidal boundaries and based on data of Grace (1973), Grace et al. (1976), Clift et al. (1978), and Bhaga and Weber (1981) for highly-deformed non-ellipsoidal boundaries at terminal conditions.

a flat surface on the bottom. The aft surface will generally be unsteady, due turbulence in the wake. At very high Weber number, such bubbles can be difficult to initiate and will tend to break up in unsteady flows. At moderate Reynolds numbers (ca. $40 < Re_p < 100$), the wake produces an approximately steady recirculation pattern with a steady aft interface, but disk-like shapes are also possible. At very high Weber numbers (>100), the bubble can form a skirt which extends downward from the spherical cap portion partially enclosing the wake. At yet lower Reynolds numbers (ca. $Re_p < 40$), the oblate ellipsoidal shape will transition into an oblate ellipsoidal cap which can include a dimple on the aft end.

For droplets in a gas ($\rho^* \gg 1$ and $\mu^* \gg 1$), increasing Weber number will transition the shape from a sphere to an oblate spheroid, similar to that seen for a bubble. However, the experimentally observed criterion for onset of ellipsoidal shapes is $We > 2$ for water drops in air, compared to $We > 0.8$ for clean bubbles. This indicates that drops in gas are less readily deformed for a given dynamic pressure, which can be attributed to their reduced internal circulation. In comparison, the strong re-circulation in a clean bubble yields surface pressure distributions closer to that of the inviscid potential flow with higher pressures in the rear and lower pressures at the sides for a given dynamic pressure (as compared to that for a sub-critical solid-sphere at the same Re_p). This translates into higher deformations for bubbles as compared to drops for a given Weber number. This also explains why contaminated bubbles exhibit less deformation than pure bubbles (Fig. 3). The differences in pressure distribution also impact shapes, e.g. the upstream portion is flatter for a drop in a gas but the aft portion is flatter for a bubble in a liquid (Clift et al., 1978). Such an interface is more susceptible to Rayleigh–Taylor interface instabilities than the rounded leading-edge surface of the spherical cap bubble. As a result, the bottom surface of drops in a gas will tend to form a dimple that can grow substantially. Eventually, a "bag" shape will be formed whereby the middle of the drop is hollowed out yielding a parachute shape which is highly unstable and will lead to break up. Taylor (1949) defined a critical Weber number that indicates the maximum stable size in quiescent conditions and is given by

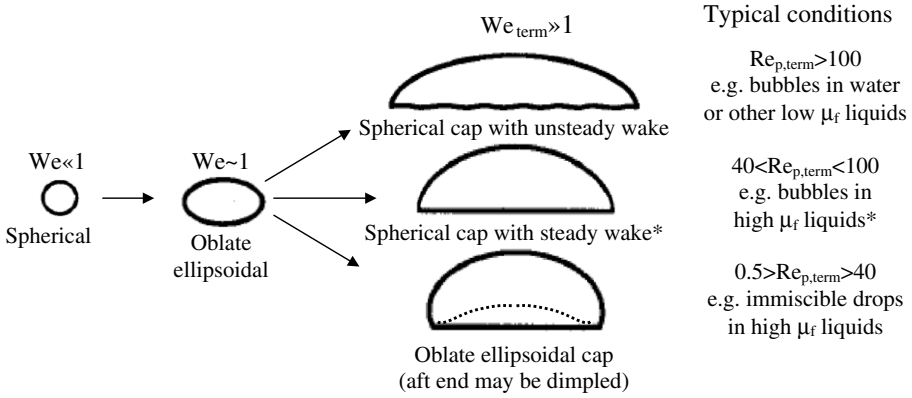

Fig. 4. Shapes of bubbles or immiscible drops in Newtonian liquids based on Grace (1973). Grace et al. (1976), Bhaga and Weber (1981), and Ryskin and Leal (1984). *Depending on density ratio, viscosity ratio, initial conditions and contamination levels, the $40 < Re_{p,term} < 100$ condition can also include other shapes such as oblate ellipsoidal disks at $10 < We_{term} < 20$ and skirted bubbles with steady or steady wakes at $We_{term} > 100$.

$$We_{crit} \approx 12 \tag{17}$$

For highly unsteady flow, the critical Weber number can be reduced (ca. 8 in turbulence). Depending on the flow dynamics, one may also observe a variety of other break-up modes, e.g. vibrational, shear, stripping, and shattering (Theofanous et al., 2004).

3.2. Terminal velocity parameters

In the above discussion, Weber number and Reynolds number were employed to describe the shape changes. While this is consistent with theoretical developments, such parameters can be difficult to measure or specify *a priori*. Because of this many experimentalists instead use the Bond number (Bo) and the Morton number (Mo) to characterize shapes at terminal velocity (w_{term}). The Bond (or Eötvös) number is proportional to particle volume

$$\mathrm{Bo} = \frac{\mathrm{g}\mathrm{d}^2|\rho_p - \rho_f|}{\sigma} \tag{18}$$

This parameter represents the ratio of effective gravitational forces to surface tension forces, where the former is proportional to the density difference between the phases and the gravitational acceleration. Note that the effective gravitational force itself does not cause deformation, e.g. a bubble which is initially released at zero velocity will have little deformation even if the Bond number is high. However, once such a bubble reaches terminal velocity, the effective gravitational forces are exactly balanced by drag, which in turn controls the relative velocity and thus the dynamic pressure that causes deformation. Thus, high Bond numbers are qualitatively similar to high We_{term}.

The Morton number is a characteristic of the multiphase fluid properties including viscosity and is given by

$$\mathrm{Mo} = \frac{g\mu_f^4|\rho_p - \rho_f|}{\rho_f^2\sigma^3} \tag{19}$$

This parameter has no direct physical interpretation, but is conveniently independent of the particle velocity or size. As such, specifying Mo and Bo does not require measurement of the particle velocity or prediction of the drag coefficient yet it allows a combination of the dynamic parameters to be specified since these four parameters are related at, but only at, the terminal velocity condition:

$$We_{term}^2/Re_{p,term}^4 = \mathrm{Mo}/\mathrm{Bo} \tag{20}$$

There are additional reasons why the Bo and Mo set are more straightforward to specify in experiments. In particular, it is straightforward to conduct measurements with Mo fixed while varying Bo (by simply changing particle size) or to keep Bo fixed and change Mo (by simply changing fluid viscosity). Similar controls are difficult to do with the *We* and Re_p parameter set. Furthermore, the gravitational effects associated with Bo and Mo help specify the hydrostatic pressure gradients at terminal conditions which influence the fore-aft shape asymmetries, i.e. non-ellipsoidal shapes which can occur at large deformations. Because of the experimental convenience, there are a wide variety correlations based on the static parameters of Bond number and/or Morton number, e.g. Harmathy (1960), (Wallis, 1974), Beard (1976), Clift et al. (1978), Ishii and Chawla (1979), Tomiyama (1998), Raymond and Rosant (2000), and Tomiyama et al. (2002)s. Such formulas are helpful to determine the *terminal* shape and velocity for a given multiphase system and particle size.

However, a limiting aspect of such correlations for shape or drag is that they can only be used to define the equilibrium conditions, i.e. when $w = w_{term}$. This is because Bo and Mo are not based on a relative velocity and are instead based on the gravity and a density difference. As such Mo and Bo can be considered "static" or "equilibrium" parameters. In contrast, *We* and Re_p are independent of gravity or the density difference and instead are functions of the relative velocity, and so can be considered "dynamic" parameters. One hybrid parameter is the Tadaki number which is equal to $Re_p\mathrm{Mo}^{0.23}$. This parameter can be considered quasi-dynamic since it includes a velocity, and perhaps because of this has been shown to

generally better than conventional "static" parameters in correlating bubble and drop shapes at terminal velocities. However, it's incorporation of gravity and a density difference indicates that its use is limited to equilibrium conditions, e.g. it would not be appropriate to describe droplet deformation caused by a high-speed horizontal injection.

In computational fluid dynamics, one generally wishes to obtain the shape and drag of fluid particles at both equilibrium and non-equilibrium conditions. This requires the use of dynamic parameters to describe the instantaneous relevant physics. To accomplish this, deformation and drag correlations have been developed herein based on We and Re_p, and is the principle contribution of this study. Another reason for choosing these parameters is that we wish to make quantitative comparison with the above cited theories.

4. Aspect ratios for clean bubbles

To analyze uncontaminated fluid particles, Taylor and Acrivos (1964) considered the geometry of deformation under the assumptions of clean conditions, linearized inertial terms, and small deformations. They obtained a first-order solution for particle shape and showed that the initial deformation is consistent with that of an oblate spheroid. The resulting aspect ratio can be expressed in terms of the particle Weber number (We) and a viscosity ratio function (λ_{μ^*}) as

$$E = \frac{1 - 2\lambda_{\mu^*} We}{1 + \lambda_{\mu^*} We} \approx 1 - 3\lambda_{\mu^*} We \tag{21a}$$

$$\lambda_{\mu^*} = \frac{1}{16(\mu^* + 1)^3}\left[\frac{81}{80}\mu^{*3} + \frac{57}{20}\mu^{*2} + \frac{103}{40}\mu^* + \frac{3}{4} - \frac{(\rho^* - 1)(\mu^* + 12)}{12}\right] \tag{21b}$$

The viscosity function does not vary significantly, i.e. λ_{μ^*} ranges from 0.052 for a bubble in a liquid ($\mu^* \to 0$) to 0.063 at for a high viscosity drop in a gas ($\mu^* \to \infty$). A correction to Eq. (21a) was also obtained by Taylor and Acrivos by including additional terms of order We^2/Re_p. The result indicated that larger deformations will give rise to non-symmetric shapes tending toward a spherical cap. The overall aspect ratio for this higher-order theory (assuming small Weber number) becomes:

$$E \approx 1 - 3\lambda_{\mu^*} We\left[1 + \frac{2(11\mu^* + 10)}{7(10\mu^* + 10)}\frac{We}{Re_p}\right] \tag{22}$$

The term in the square brackets indicates the higher-order correction.

Quantitative comparisons of the aspect ratio at relatively low Reynolds numbers ($0.2 < Re_p \leqslant 2$) against data of clean bubbles ($\mu^* \to 0$) from experiments and resolved-surface simulations are shown in Fig. 5. The aspect ratio predicted by the Taylor–Acrivos theory (Eq. (21a)) is reasonable for all these Reynolds numbers up to $We < 0.5$, beyond which it tends to over-predict the deformation. This is consistent with detailed shape comparisons by Ryskin and Leal (1984). The higher-order Taylor–Acrivos theory (Eq. (22)) is also shown for $Re_p = 1$ and is reasonable within its theoretical limits of $Re_p \ll 1$ and $We^2/Re_p \ll 1$. At higher Weber numbers, the aspect ratio tends to reach a constant minimum value ($E_{min} = E_{We \to \infty}$). The minimum aspect ratio can be difficult to determine since there is scatter in the measurements (since instabilities can arise) and the simulations (attributed to the computational complexity of handling large deformations). However, an approximate correlation for the aspect ratio of uncontaminated bubbles can be constructed as

$$E = 1 - (1 - E_{min})\tanh(c_E We) \tag{23}$$

Based on data for pure bubble systems over a range of Reynolds numbers from 0.2 to 5000 (shown in this and in the following plots), E_{min} and c_E can be modeled as

$$E_{min} = 0.25 + 0.55\exp(-0.09 Re_p) \tag{24a}$$

$$c_E = 0.165 + 0.55\exp(-0.3 Re_p) \tag{24b}$$

Comparison with $Re_p = 1$ is shown in Fig. 5 where the fit approaches that of the Taylor–Acrivos theory at low Weber numbers, and higher Re_p conditions will be shown in the following figures.

There are three main points regarding this result. Firstly, the number of data points available for these conditions is rather small since deformation at these Reynolds numbers requires extremely viscous liquids and is generally weak, and since much of the experimental data in the literature did not include measurements of the relative velocity needed for determine the Weber number. Even when the relative velocity could be extracted, it was sometimes associated with measurement uncertainty which (along with potential effects of contamination) contributed to the scatter of the data. As such, the empirical aspect ratio equation given above may only be approximate for high Weber numbers and low Reynolds numbers. Secondly, creeping flow conditions will generally yield only weak or negligible deformation, i.e. $E_{min} \sim 1$ for $Re_p < 0.1$ (Eq. (15)). Thirdly, the above expressions assume that the shape is a function of the local We and Re_p and is not undergoing unsteady deformation. For most flows, this is a reasonable assumption since the natural frequency of the bubble shape oscillations is on the order of several kHz (for diameters of 20 cm or less) so that the shapes adapt almost immediately to the local flow conditions.

For moderate Reynolds numbers (ca. $1 < Re_p < 100$), there is no theoretical solution for the aspect ratio and instead empirical expressions must be employed. For these conditions, Bhaga and Weber (1981) conducted experiments of deforming bubbles in high-viscosity uncontaminated liquids ($0.004 < Mo < 850$) and concluded that bubble shape is primarily a function of Re_p (and not We). However, experiments and simulations (Ryskin and Leal, 1984; Kojima et al., 1968; Raymond and Rosant,

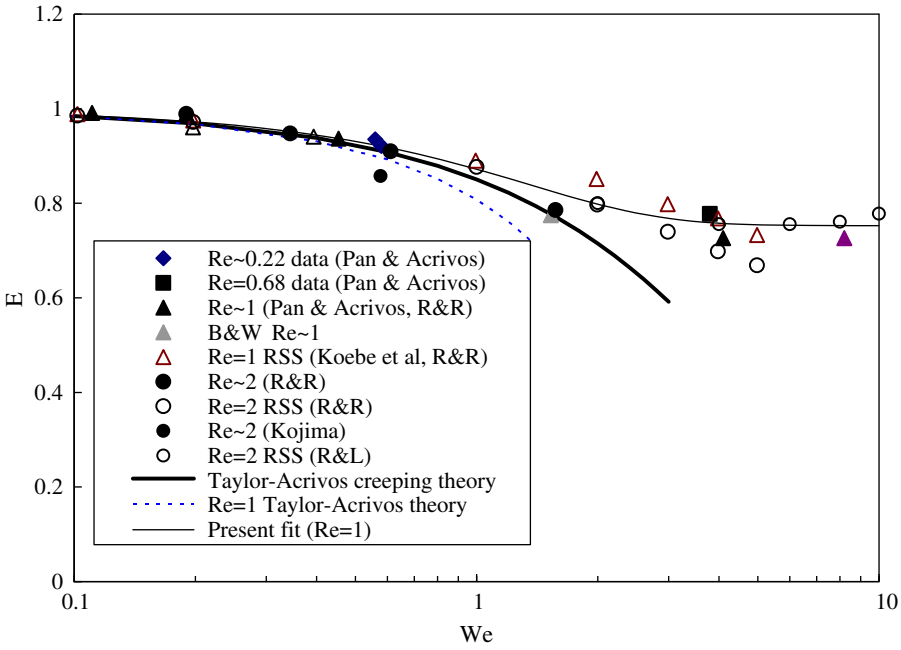

Fig. 5. Aspect ratios at low particle Reynolds numbers ($Re_p \leqslant 2$) based on experiments, RSS, theory (Koebe et al., 2003; Kojima et al., 1968; Pan and Acrivos, 1968; Raymond and Rosant, 2000; Ryskin and Leal, 1984) and an empirical fit for uncontaminated bubbles.

2000) have shown that Weber number effects are also important. Results from these studies are shown in Fig. 6 along with the fit of Eq. (23). While there is some scatter, the data for a given Reynolds number tend to collapse as a function of Weber number with an initial trend similar to that of the Taylor–Acrivos theory followed by a leveling off at E_{min} (all of which tends to follow the empirical fit). As in Fig. 5, the value of E_{min} decreases as the Reynolds number increases. This is attributed to the increased importance of inertia terms which cause further deformation by creating a high pressure on the front and rear and a low pressure on the sides. However, the aspect ratio only describes a gross feature of the bubble shape since the shape is no longer spheroidal at high deformations. For example, the bubble trailing-edge forms a dimple at Re_p of about 3 which peaks in magnitude at Re_p of about 40 and then disappears at Re_p of about 100 (Bhaga and Weber, 1981; Ryskin and Leal, 1984). Furthermore, the data in Fig. 6 exclude the disk and skirted bubble shapes which occur at $We > 100$ for this Re_p range (Clift et al., 1978).

At high Reynolds numbers, Moore (1965) obtained theoretical deformations for clean bubbles at low Weber numbers. In particular, he assumed that the viscous flow over the bubble was confined to a thin boundary layer which remains attached. Blanco and Magnaudet (1995) conducted several simulations and showed that the boundary between attached and separated wakes for deforming clean bubbles is a function of Re_p and E as shown in Fig. 7. This figure also includes two sample streamline simulations on either side of this boundary, whereby the larger We condition yields a wake vortex. The data of the terminal velocity conditions for air bubbles in hyper-clean water of Duineveld (1995) indicate that the flow may be attached for E as low as 0.55, consistent with observations by Moore.

Moore's low order theory for deformation is based on a pressure distribution arising from irrotational flow over a stress-free spherical surface. Assuming a small Weber number, this yields an oblate spheroid with an aspect ratio:

$$\frac{1}{E} = 1 + \frac{9}{64} We \tag{25}$$

Moore also obtained a higher-order approximation by employing the potential flow solution over an oblate ellipsoid (Lamb, 1945) which resulted in an implicit relationship for aspect ratio as a function of Weber number

$$We = \frac{4E^{1/3}(1 + E^2 - 2E^3)}{(1 - E^2)^3}\left(E\sqrt{1 - E^{-2}} - \cos^{-1} E\right)^2 \tag{26}$$

For moderate deformations ($E > 0.5$), this relationship can be approximated explicitly as

$$\frac{1}{E} \approx 1 + \frac{9}{64} We - 0.0089 We^2 + 0.0287 We^3 \tag{27}$$

The average difference between this result and Eq. (26) is 0.3% for $E > 0.5$, so that Eq. (27) is generally reasonable for the entire attached flow regime (Fig. 7).

Predictions of aspect ratio as well as results from experiments and RSS for $Re_p \geqslant 100$ are shown in Fig. 8. The results indicate that both the low-order theory (Eq. (25)) and the high-order theory (Eqs. (26) or (27)) are quite reasonable for small We, consistent with Moore's assumptions. It is interesting that the experimental and RSS

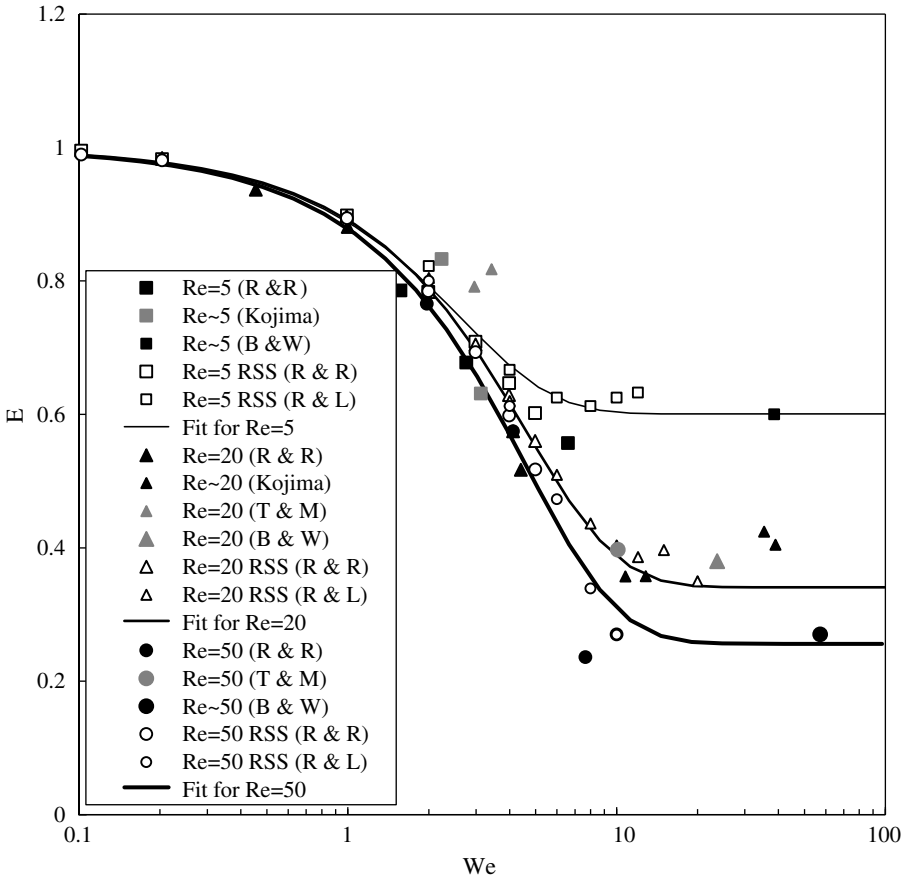

Fig. 6. Aspect ratios at moderate particle Reynolds numbers for uncontaminated bubbles.

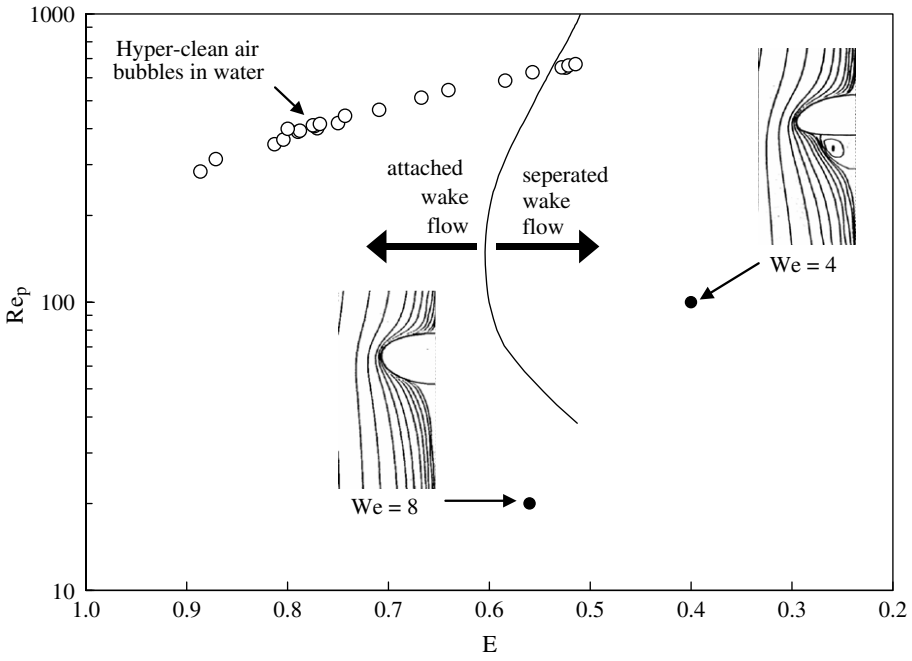

Fig. 7. Prediction pure bubble of flow attachment or separation boundary by Blanco and Magnaudet (1995) and streamline simulations of Takagi et al. (1994), and hyper-clean bubbles of Duineveld (1995).

results for E tend to be bounded by the two theories at moderate Weber numbers, but then tend to a minimum value independent of Re_p. Also shown in Fig. 8 is the empirical relationship for the aspect ratio in this regime

based on Eq. (23). This corresponds well with Moore theory at low *We* values, though the aspect ratio of bubbles in water tends to be somewhat over-predicted by the empirical result. This may be due to the difficulty of obtaining a completely uncontaminated surface for water as discussed above.

Note that the theories are no longer suitable for $E < 0.5$ since they do not account for the open-wake which develops and since they predict $E \to 0$ as the surface tension becomes weak. In practice, bubbles with $E < 0.5$ differ substantially from an ellipsoid (as the fore-aft symmetry is broken) and at maximum-deformation tends toward an (approximate) universal minimum given by Eq. (23), i.e.

$$E_{We\to\infty} \sim 0.25 \qquad \text{for } Re_p > 100 \tag{28}$$

This limit is consistent with oblate spherical-cap bubbles and has been pointed out by several researchers for high Re_p conditions (Clift et al., 1978). While there has not been success for a direct quantitative theoretical prediction of Eq. (28), the interface geometry can be qualitatively obtained at terminal velocity conditions by neglecting surface tension and viscosity. In particular, the spherical segment is consistent with a nearly inviscid pressure distribution balanced by hydrostatic pressure variations while the nearly flat aft end of the bubble is consistent with the air pressure equal to local hydrostatic pressure. As such, the fore-aft (non-ellipsoidal) asymmetry in terminal conditions is related to hydrostatic pressure (and not just hydrodynamic pressure). However, Eqs. (22), (23) and (27) can take this effect into account since We_{term} and $Re_{p,term}$ specify the Bo and Mo though Eq. (20) and $C_{D,term}$.

Since the above correlations are functions of the instantaneous Weber number, they would be expected to be appropriate at velocity conditions which are not necessarily the mean rise velocity. To test this, predictions of aspect ratio were compared to experimental data of bubbles rising in clean water whereby the trajectory oscillations lead to relative velocity variations. Sample comparisons are shown in Fig. 9 where the agreement is reasonable though the variation amplitude tends to be somewhat predicted.

5. Drag of deformed clean bubbles

Increasing the bubble or drop size at terminal conditions (as in Fig. 2), will result in an increase in Re_p, which by itself is known to reduce C_D for a spherical shape, e.g. via Eqs. (7) or (11). However, if this increase in size also corresponds to a transition to an ellipsoidal shape, the

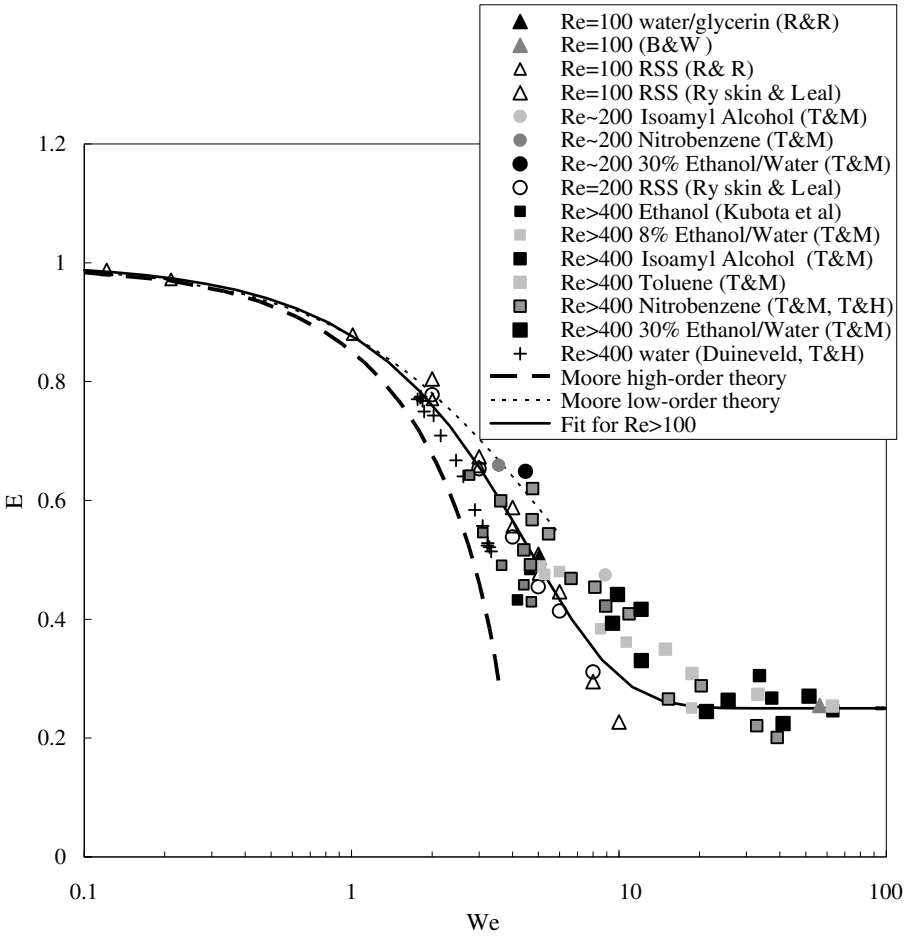

Fig. 8. Aspect ratios at high particle Reynolds numbers (>100) for uncontaminated bubbles.

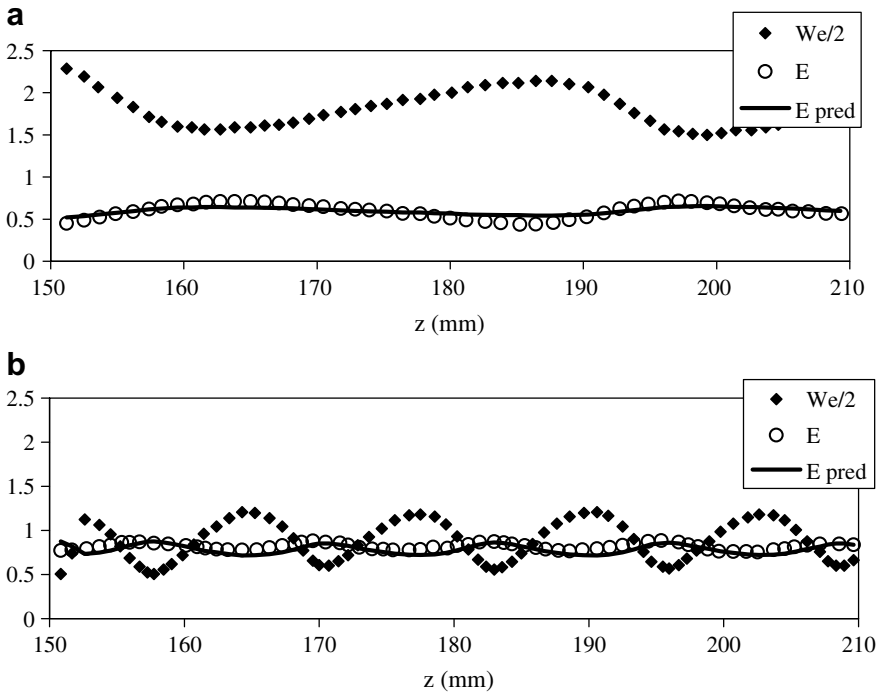

Fig. 9. Measured aspect ratio and Weber number (vertical axis of plot) for 2.5 mm diameter clean bubbles as a function of the vertical rise location (horizontal axis of plot) obtained by Tomiyama et al. (2002) compared with aspect ratio predictions based on Fig. 8: (a) helical motion and (b) zig-zag motion.

increase in frontal area and an increased probability of wake separation will cause an increase in C_D for a given Re_p. As shown in Fig. 10, the combined result of these two effects can be either an increase or a decrease in $C_{D,term}$ depending on the type of fluid particle. For example, the onset of deformation with increasing $Re_{p,term}$ shows a rapid rise in $C_{D,term}$ for clean bubbles but an initial decrease for contaminated bubbles. In the following, these two competing effects will be separated by considering the impact of Weber number for a fixed particle Reynolds number, consistent with theoretical approaches.

There are three limiting conditions where drag can be theoretically obtained for clean fluid particles: (a) linearized inertia and small deformation ($Re_p \ll 1, We \ll 1$), (b) bubbles with thin boundary layers, attached wake and small deformations ($Re_p \gg 1, We \ll 1$), and (c) spherical-cap bubbles with a separated wake ($Re_p \gg 1, We \gg 1$). Each is discussed in the following, and then later are used for a generalized bubble (and droplet) drag for arbitrary μ^*, Re_p and We.

Including only linearized inertial terms, Taylor and Acrivos (1964) used the low Re_p theoretical deformation of Eq. (20) to obtain the drag for an oblate spheroid along the axis of symmetry. To do this they extended the spherical stream function work of Proudman and Pearson (1957) by assuming small departures from a spherical shape. From the stream function solution, the friction and form drag could be obtained. Neglecting terms of order $Re_p^2 \ln Re_p$, their result can be expressed in terms of the Stokes correction factor as

$$f_{\parallel} = \frac{2+3\mu^*}{3+3\mu^*} + \frac{3}{16} Re_p \left(\frac{2+3\mu^*}{3+3\mu^*}\right)^2 + \lambda_{\mu^*} We \frac{6}{5} \times \frac{(8+3\mu^{*2}-\mu^*)}{(3+3\mu^*)^2} \tag{29}$$

The first two terms on the RHS are the corrections obtained for spherical fluid particles in linearized flow (Eq. (9)) while the last term is due to deformation. At low Reynolds numbers (where the second term is neglected), the Stokes correction approaches $f = 2/3 + 0.055\ We$ for bubbles ($\mu^* \ll 1$) and $f = 1 + 0.025\ We$ for drops in a gas ($\mu^* \gg 1$), indicating that bubbles are more sensitive to deformation changes than are drops. In either case, significant changes occur for Weber numbers greater than 0.1.

Drag for the second condition (an attached boundary layer over the entire bubble surface with weak deformation) was obtained by Moore (1965) by assuming an oblate ellipsoid with the aspect ratio given by Eq. (26). The (outer) potential flow solution was obtained (assuming inviscid flow) to find the dissipation associated with a thin boundary layer consistent with the stress-free condition. From this, the drag can be obtained to order $Re_p^{1/2}$ as

$$C_{D,Moore} = \frac{48}{Re_p} G_E \left(1 - \frac{2.21 H_E}{Re_p}\right) \tag{30}$$

The parameters G_E and H_E are functions of the aspect ratio. The first can be given directly as

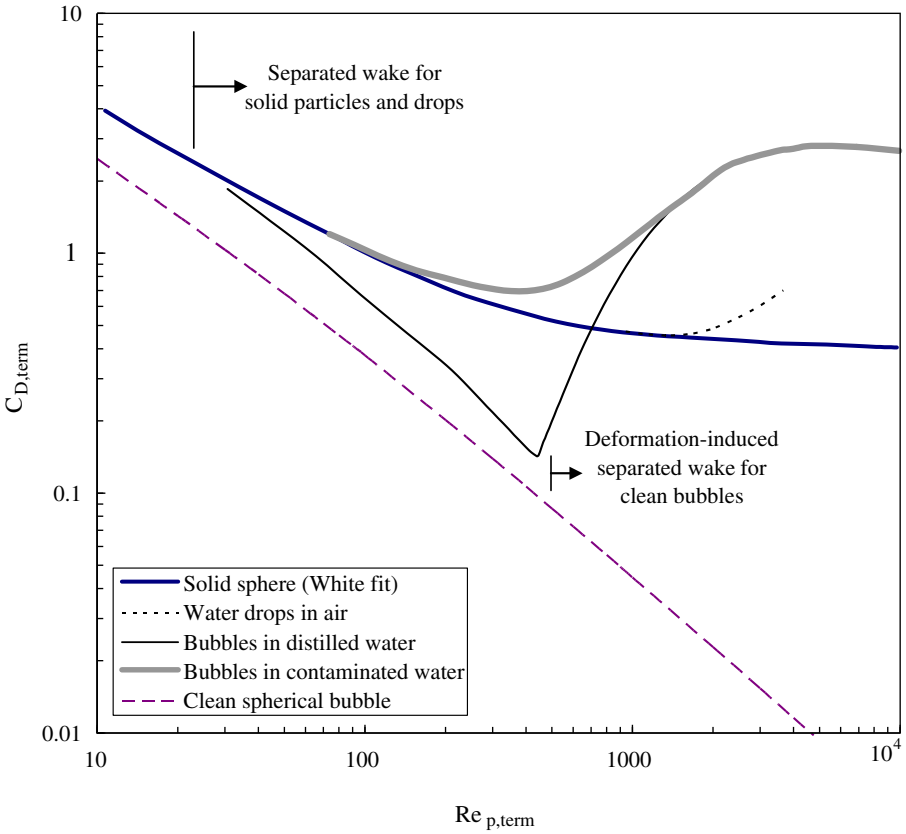

Fig. 10. Terminal drag coefficients for solid and fluid particles based on data of Fig. 2.

$$G_E = \frac{E^{-7/3}}{3}(1-E^2)^{3/2}\frac{E\sqrt{1-E^2}+(1-2E^2)\cos^{-1}E}{\left(E\sqrt{1-E^2}-\cos^{-1}E\right)^2} \quad (31)$$

This function can also be approximated for $E > 0.5$ (attached flow conditions) as

$$G_E \approx 0.1287 + \frac{0.4256}{E} + \frac{0.4466}{E^2} \quad (32)$$

The second function must be numerically obtained and a table of values is given by Moore (1965); though a more convenient approximation for $E > 0.5$ is

$$H_E \approx 0.8886 + \frac{0.5693}{E} - \frac{0.4563}{E^2} \quad (33)$$

The drag of Eq. (30) reverts to the spherical form (Eq. (10)) as E approaches unity, i.e. $G_E \to 1$ and $H_E \to 1$. Moore also points out that the contribution of H_E becomes negligible at sufficiently high Re_p values, though this requires Mo on the order of 10^{-14} or less for terminal conditions. Note that these results are unreasonable for conditions of flow separation (Fig. 7), an issue which will be addressed below.

The third theoretical result (Davies and Taylor, 1950) is for a spherical-cap bubble for which surface tension boundary layer effects can be ignored and the bubble Reynolds number is high. The latter aspect allows the pressure just above the spherical-segment of the bubble to be approximated from potential theory, which must be balanced by the hydrostatic effect yielding

$$C_D = \frac{8}{3} \quad \text{for} \quad We \to \infty \quad \text{and} \quad Re_p \to \infty \quad (34)$$

This well-known Davies and Taylor result has been found to reasonably represent drag on spherical-cap bubbles at high Re_p (Clift et al., 1978). Joseph (2006) extended this result in manner similar to Moore (1965) to include viscous effects yielding:

$$C_D = \frac{8}{3} + \frac{14.24}{Re_p} \quad \text{for} \quad We \to \infty \quad \text{and} \quad Re_p \gg 1 \quad (35)$$

However, the additional term is generally less than 1% for most spherical cap bubbles as they occur at high Re_p values, so that Eq. (34) is often reasonable. As will be discussed later, there is experimental evidence that $C_D \approx 8/3$ is also reasonable for disintegrating drops as $We \to \infty$ (Simpkins and Bales, 1972) and may thus be reasonable at all viscosity and density ratios at high Re_p conditions.

To bridge wide range of small to large Reynolds numbers, Darton and Harrison (1974) and Clift et al. (1978) proposed an empirical expression for the maximum-deformation C_D by linearly combining the creeping flow drag of Eq. (19) with the $Re_p \gg 1$ drag of Eq. (34):

$$C_{D,\max} = C_{D,We\to\infty} \approx \frac{8}{3} + \frac{24}{Re_p}\left(\frac{2+3\mu^*}{3+3\mu^*}\right) \quad (36)$$

The above theoretical results and the empirical result of Eq. (36) are evaluated with experiments and direct simulations of bubble drag coefficient as shown in Fig. 11 for various Re_p values as a function of Weber number. As may be expected, the Taylor–Acrivos theory is reasonable for $Re_p < 1$ and $We < 1$, but tends to overestimate the drag for higher Re_p or We. As also expected, the Moore theory is reasonable for $We < 4$ and Mo = 4.45E-10 (which corresponds to $Re_p > 100$ and $E > 0.5$). However, it underestimates the drag at higher Weber numbers, which can be attributed primarily to the onset of a separated wake. At $We \gg 1$ for this condition, the drag coefficient tends to approach an equilibrium value consistent with the spherical-cap theory of Eq. (34). For Re_p values as low as 2, Eq. (36) gives a remarkably robust prediction of the maximum-distortion drag coefficient.

To correlate the drag at intermediate Re_p and We values, a normalized drag coefficient increment can be defined (similar to that used in Eq. (12)) as

$$\Delta C_D^* \equiv \frac{C_D - C_{D,We\to 0}}{C_{D,We\to\infty} - C_{D,We\to 0}} \tag{37}$$

For clean bubbles, $C_{D,We\to 0}$ is given by the spherical case of Eq. (11) whereas $C_{D,We\to\infty}$ is given by the spherical-cap case of Eq. (36). When plotted as a function of We, data from experiments and RSS can be primarily grouped in terms of $Re_p > 100$ and $Re_p < 100$.

Considering first the category of $Re_p > 100$, one can employ Moore's theory (Eqs. (30) and (23)) to obtain the drag increment at moderate Weber numbers. This gives good predictions for the attached flow region for liquids of various Morton numbers (Fig. 12). For the separated regime, Mendelson (1967) noted that the terminal velocity was approximately independent of Re_p and instead dominated by surface tension and gravitational effects. He then considered the bubble as an interfacial surface wave disturbance and equated the wavelength to the bubble perimeter to obtain the terminal velocity as $w_{term} = \sqrt{2\sigma/\rho_f d + gd/2}$. This result can be expressed in terms of the terminal Weber number for a bubble as

$$C_{D,term} = \frac{8}{3}\left(\frac{We_{term} - 2}{We_{term}}\right) \tag{38}$$

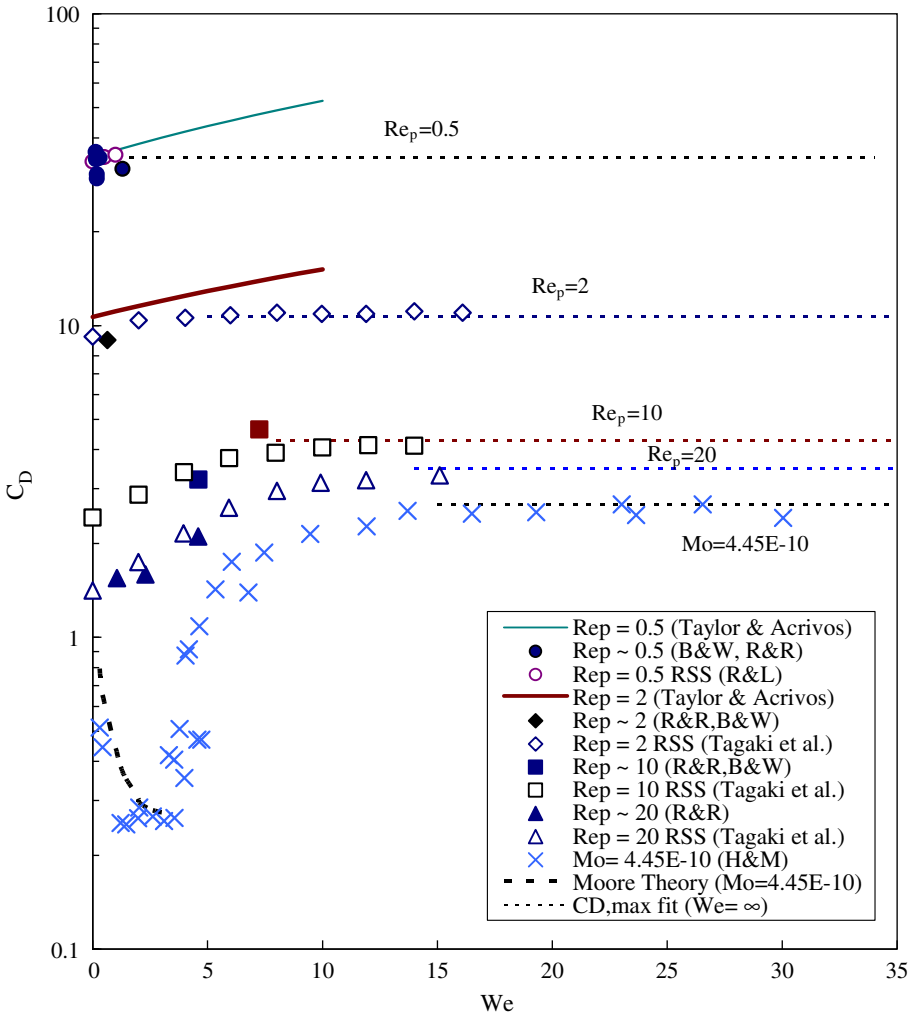

Fig. 11. Drag coefficients of uncontaminated bubbles at low to moderate Reynolds numbers.

Clift et al. (1978) and Fan and Tsuchiya (1990) considered minor variations of this expression (e.g. the value of 2 was replaced by 3 or other numbers). Another, and perhaps better, empirical correlation (as shown in Fig. 12) for this separated regime is given by

$$\Delta C^*_{D,\ \text{separated}} \approx 2.5\tanh(0.2We) - 1.5 \tag{39}$$

A shown in Fig. 12, the separated drag is appropriate for $We > 5$ while the Moore drag is appropriate for $We < 3$. For intermediate conditions ($3 < We < 5$), a simple approximation is to use the maximum value:

$$C_D \approx \max(C_{D,\text{Moore}}, C_{D,\text{separated}}) \qquad \text{for} \quad Re_p > 100 \tag{40}$$

This combination gives good predictions as shown in Fig. 12. Note that the demarcation between the attached and separated regimes is responsible for the peak in terminal velocity seen in Fig. 2 for bubbles in distilled water.

Measurements and RSS results for the intermediate Re_p condition of $5 < Re_p < 100$ are shown in Fig. 13 where it can be seen that they approximately collapse as a single function given by

$$\Delta C^*_D \approx \tanh(0.021We^{1.6}) \qquad \text{for} \quad 5 < Re_p < 100 \tag{41}$$

There is significant scatter in the data and potentially an additional influence of viscosity associated with variations of Re_p or Mo such that this correlation may be considered qualitative. However, the relative change in drag in this regime ($\Delta C_D/C_{D\max}$) can be small, e.g. about 30% at Re_p=5. As such any scatter in C_D will be exaggerated when considered in terms of ΔC^*_D at these conditions.

For $Re_p < 5$, the Taylor–Acrivos theory initially applies at small We but soon after the drag coefficient saturates at the maximum-deformation value which is typically only a few % higher than the spherical value (see Fig. 13). It is difficult to assess an appropriate ΔC_D for $Re_p < 5$ because: (a) the C_D variations are small, (b) shapes may be sensitive to initial conditions and (c) the experimental data are scant (Fig. 11). However, Eq. (41) is at least qualitatively correct. To overview the performance of the above methods, the measured drag coefficients for a variety of liquid are shown in Fig. 14 based on:

$$C_{D,\text{term}} = \frac{4}{3}\frac{\text{Bo}}{We} = \frac{4}{3}\text{Mo}\frac{Re^4_{p,\text{term}}}{We^3_{\text{term}}} \tag{42a}$$

This figure also shows the results of Eqs. (40) or (40) combined with Eqs. (11) and (36) via Eq. (37), i.e.

$$C_D = \frac{24}{Re_p} f_{Re,\mu^*\to 0} + \Delta C^*_D(C_{D,We\to\infty} - C_{D,We\to 0}) \tag{42b}$$

These predictions are generally accurate and robust indicating that drag of clean bubbles which are deformed by relative velocity can be reasonably characterized by dynamic parameters such as We and Re_p.

Shows measured terminal drag coefficients for a wide variety of liquids processed according to:

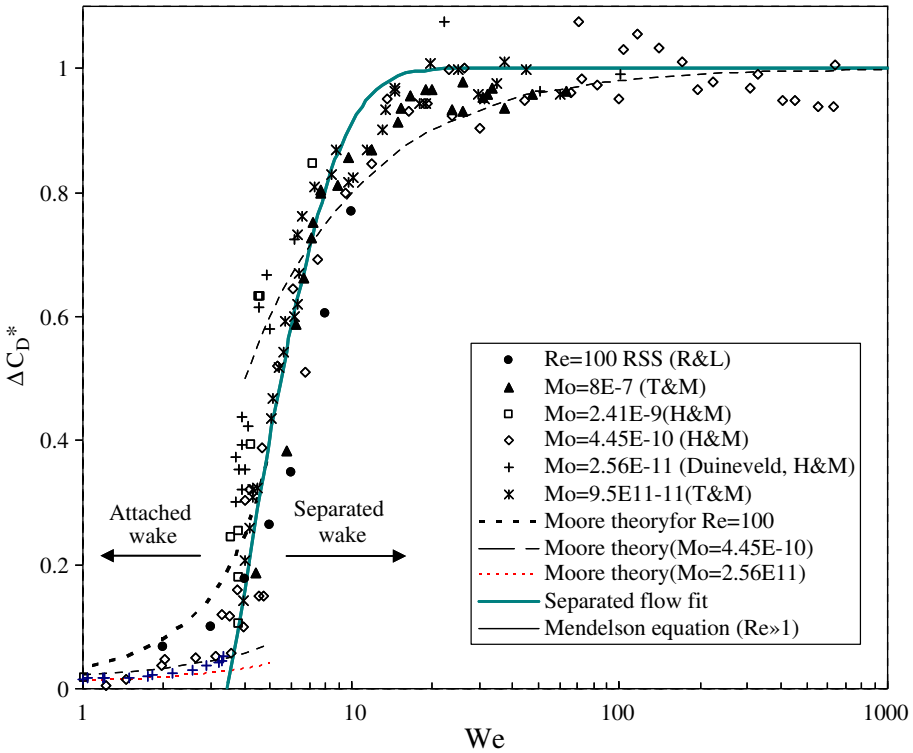

Fig. 12. Incremental drag coefficient for uncontaminated bubbles at high Reynolds number ($Re_p > 100$) based on data from Haberman and Morton (1953), Tadaki and Maeda (1961), and Duineveld (1995).

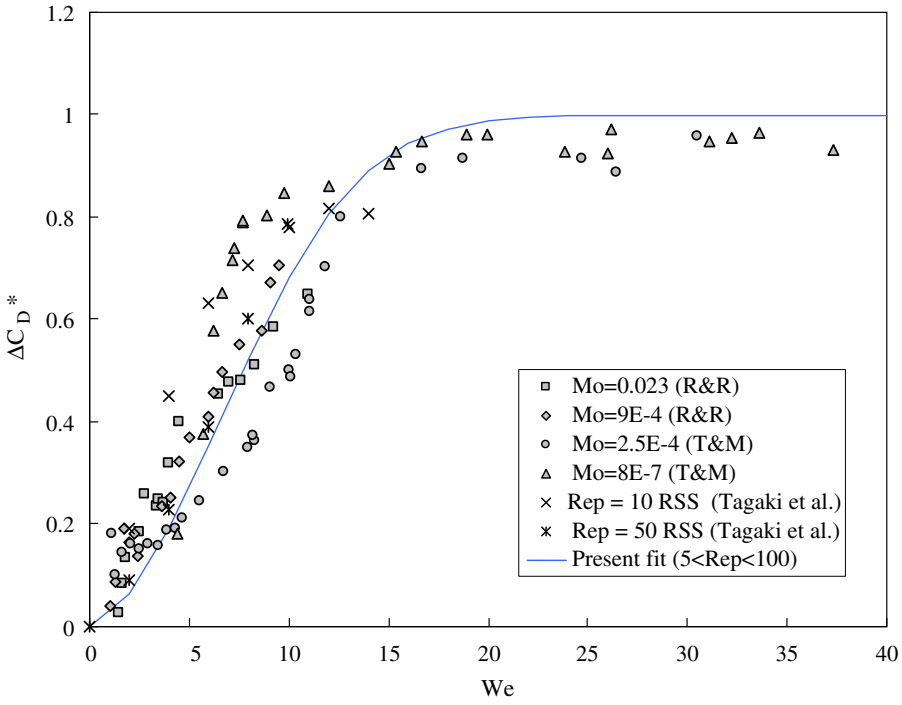

Fig. 13. Incremental drag coefficient for uncontaminated bubbles at moderate Reynolds numbers based on data from Tadaki and Maeda (1961), Bhaga and Weber (1981), and Raymond and Rosant (2000) as well as RSS results from Takagi and Matsumoto (1999).

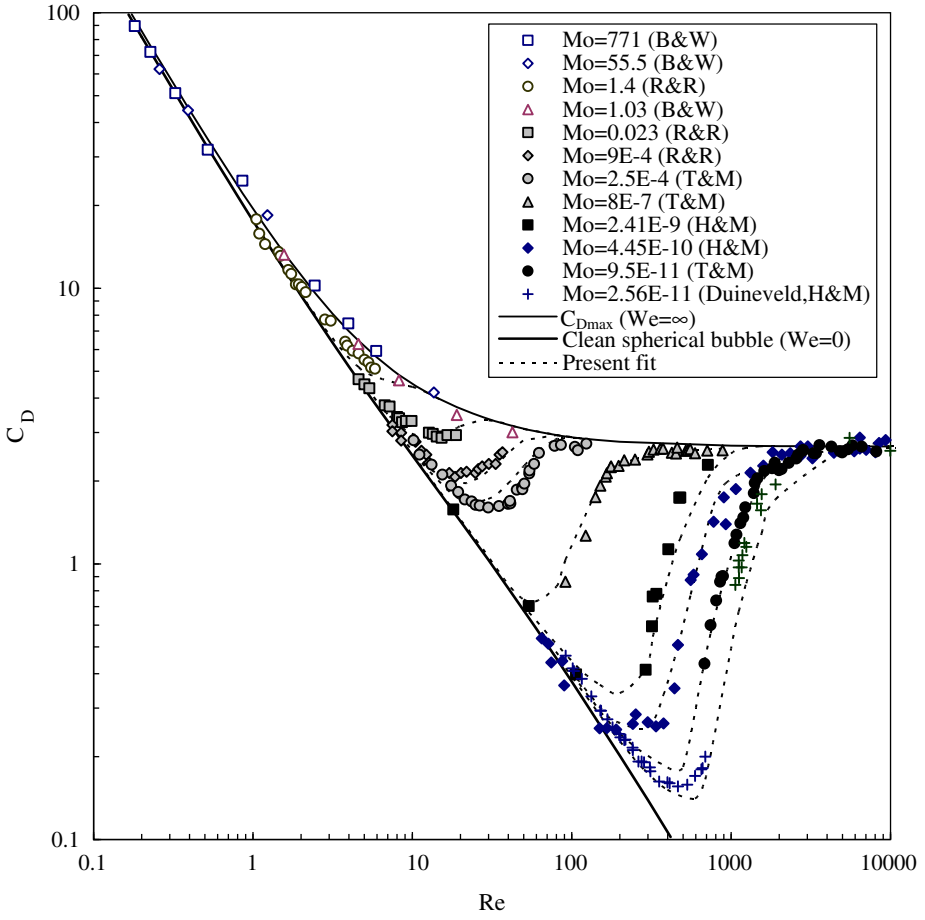

Fig. 14. Terminal drag coefficients for various Morton numbers of uncontaminated bubbles.

$$C_{D,term} = \frac{4}{3}\frac{Bo}{We} = \frac{4}{3}Mo\frac{Re_p^4}{We^3} \quad (42)$$

The predictions of Eqs. (11), (36), (39) and (40) are generally accurate and robust indicating that drag of pure bubbles (deformed by relative velocity) can be reasonably characterized by dynamic parameters such as We and Re_p.

6. Aspect ratios and drag for drops in a gas

For quasi-steady conditions, one can expect the shape of a drop in a gas to be dominated by the instantaneous Weber number. Unfortunately, there is no quantitative theory for deformation (or drag) for drops in a gas. This is because the flow over the surface is generally separated since the high-viscosity ratio results in nearly a no-slip boundary condition and since deformation typically occurs at $Re_p > 1000$ (Fig. 2). As such, one must rely upon empirical correlations. Experiments for drops of different liquids in different gas pressures were carefully studied by Reinhart (1964). While he developed a Bond number correlation, the resulting aspect ratios correlate well with Weber number as shown in Fig. 15 and can be characterized by the empirical fit

$$E = 1 - 0.75\tanh(0.07We) \quad \text{for} \quad We < We_{crit} \quad (43)$$

While this is not intended for $We > We_{crit}$, photographs of drops which are disintegrating due to shock waves at very high Weber numbers (>1000) indicate an instantaneous lenticular shape with surface stripping with a main body aspect ratio of approximately 1/4, consistent with the limit of this correlation (Simpkins and Bales, 1972; Theofanous et al., 2004).

The normalized drag increment (based on Eqs. (6), (36), (37)) for a drop in a gas corresponds well with the dimensionless group $WeRe_p^{0.2}$ as shown in Fig. 16. Note that the 0.2 exponent was empirically determined to give best data collapse and that this group can be rewritten in terms of the We, ρ^*, μ^*, and the Ohnesorge number (ratio of viscous stresses to surface tension stresses). The data trends can also be approximated with the following dependence:

$$\Delta C_D^* \approx 3.8\times10^{-3}\left(WeRe_p^{0.2}\right) + 3\times10^{-5}\left(WeRe_p^{0.2}\right)^2 + 9\times10^{-7}\left(WeRe_p^{0.2}\right)^3 \quad (44)$$

This increment only applies to $We < We_{crit}$ (since it becomes unbounded for $We \to \infty$), while the drag of drops disintegrating by shock waves is better correlated with Eq. (34) (Fig. 17). As such, there may be an instantaneous drag increment for intermediate We as suggested by the dashed line of Fig. 16, but there is insufficient data for quantitative determination. To summarize the drag coefficient prediction for drops in gas, Fig. 17 presents data and predictions for falling drops (based on Eq. (44)) and disintegrating drops (based on Eq. (36)), where it is seen that the expressions are reasonably robust for a wide range of conditions ($400 < Re_p < 7000$).

7. Aspect ratios and drag for contaminated bubbles and drops in liquids

Like drops in a gas, contaminated bubbles and drops in liquids yield a separated wake for even modest Re_p values so that no theoretical solutions for the deformation and drag are available, and again we must rely upon experimental evidence and empirical correlations. For the aspect ratio

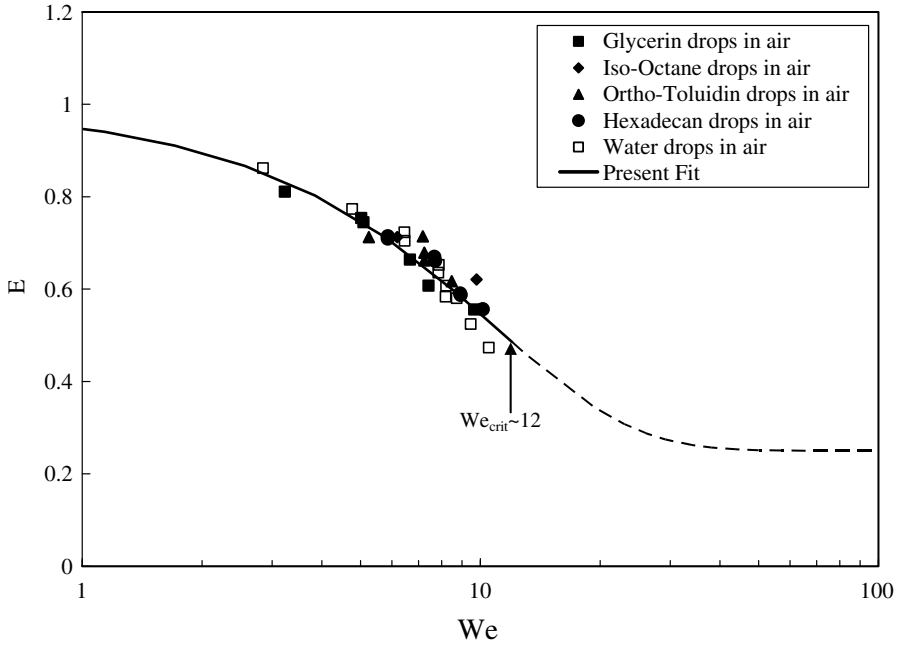

Fig. 15. Aspect ratio for deformable drops in air for $Re_p > 600$ based on experimental data of Reinhart (1964).

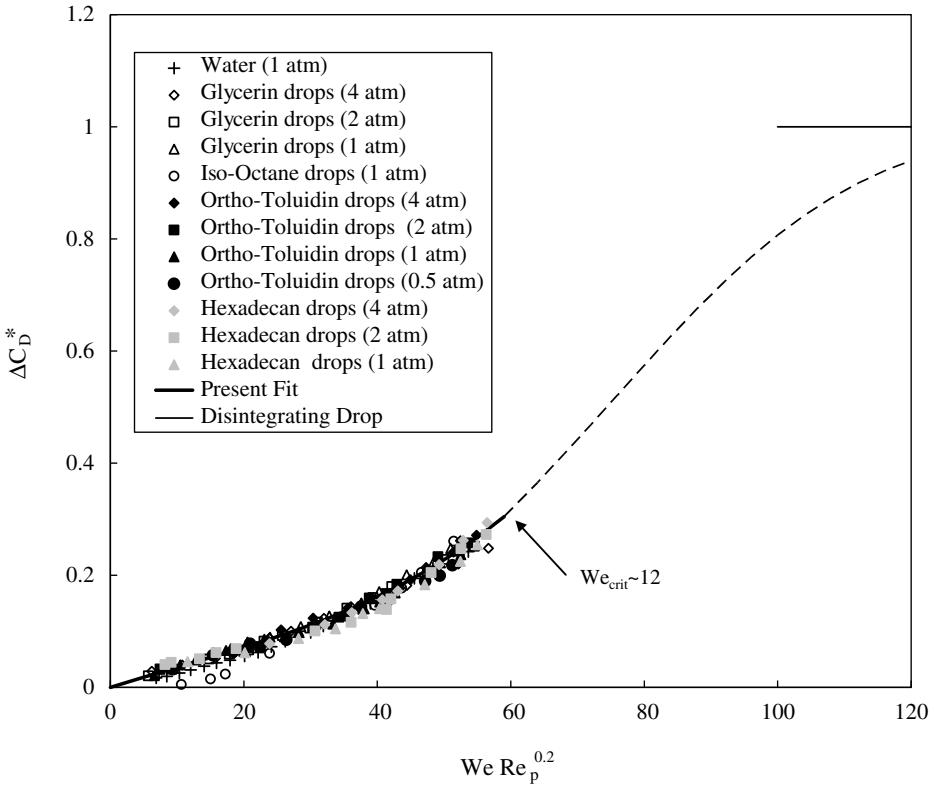

Fig. 16. Incremental drag coefficient ratio for drops in air at various pressures (Reinhart, 1964).

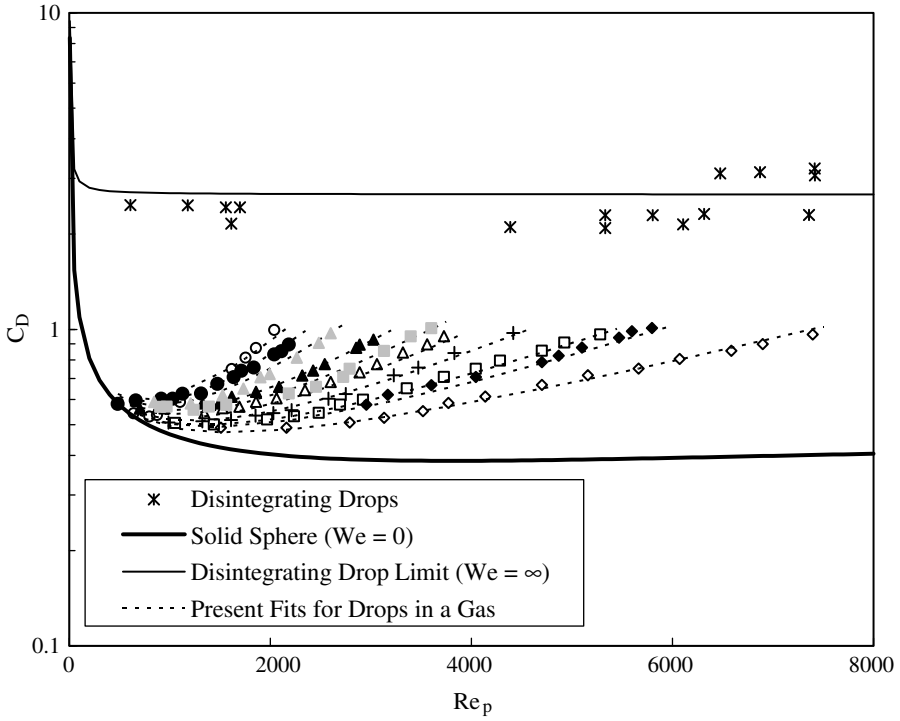

Fig. 17. Drag coefficient as a function of Reynolds number for terminal conditions (see legend in Fig. 16) and for disintegrating drops (Simpkins and Bales, 1972).

trends, there is reasonable correlation with Weber number for a wide variety of drop and bubble conditions as indicated in Fig. 18, whereby the results can be approximated (ca. within ±5%) as

$$E = 1 - 0.75\tanh(0.11We) \quad (45)$$

This Weber number dependence is qualitatively similar to the results for other fluid particle cases in that the minimum aspect ratio tends to 0.25. However, there are some significant differences which can be gleaned by comparing Fig. 18 to Figs. 8 and 15. Firstly, deformations for contaminated fluid particles are less sensitive to Weber number as compared to pure bubbles in a liquid. This effect can be partially attributed to the increased velocity and, therefore, lower pressure at the sides of bubbles for stress-free (vs. no-slip) boundary conditions. A second difference is that deformation for drops in liquids is more sensitive to Weber number than that for drops in a gas. This effect may be related to differences in ρ^* whereby drops in a liquids are not as influenced by hydrostatic pressure gradients, a trend which is similar to that predicted for low Re_p conditions Eq. ((20)).

A third difference is that pure and contaminated bubbles can achieve steady-state spherical-cap shapes at high We values, whereas drops in liquids and drops in gas tend to break up by a We_{crit} of about 12. This effect is attributed to differences in ρ^* since droplet mass undergoing asymmetric shape oscillations has substantial inertia moving in different directions which can more easily overcome the restoring surface tension. In contrast, the interior fluid of bubbles has negligible inertia so that the interface shape dynamics are instead governed by internal pressure and the surrounding fluid. However, bubbles can still be unstable at have difficult maintaining high We conditions. For example, Davies and Taylor (1950) noted "significant difficulty" in creating the initial conditions for large spherical-cap bubbles, lest they break up into smaller bubbles. In fact, contaminated bubbles tend to be constrained to $We < 10$ (Fan and Tsuchiya, 1990). Furthermore, E_{min} is not universal since toroidal bubbles can form at high We depending on the initial conditions (Bonometti and Magnaudet, 2006) while skirted bubbles can form at $We > 100$ and skirted drops at $We > 10$ at intermediate Reynolds numbers (Clift et al., 1978).

The incremental drag for contaminated bubbles and drops can be constructed in a manner similar to that for drops in a gas (using Eqs. (6), (36), and (37)) and correla-

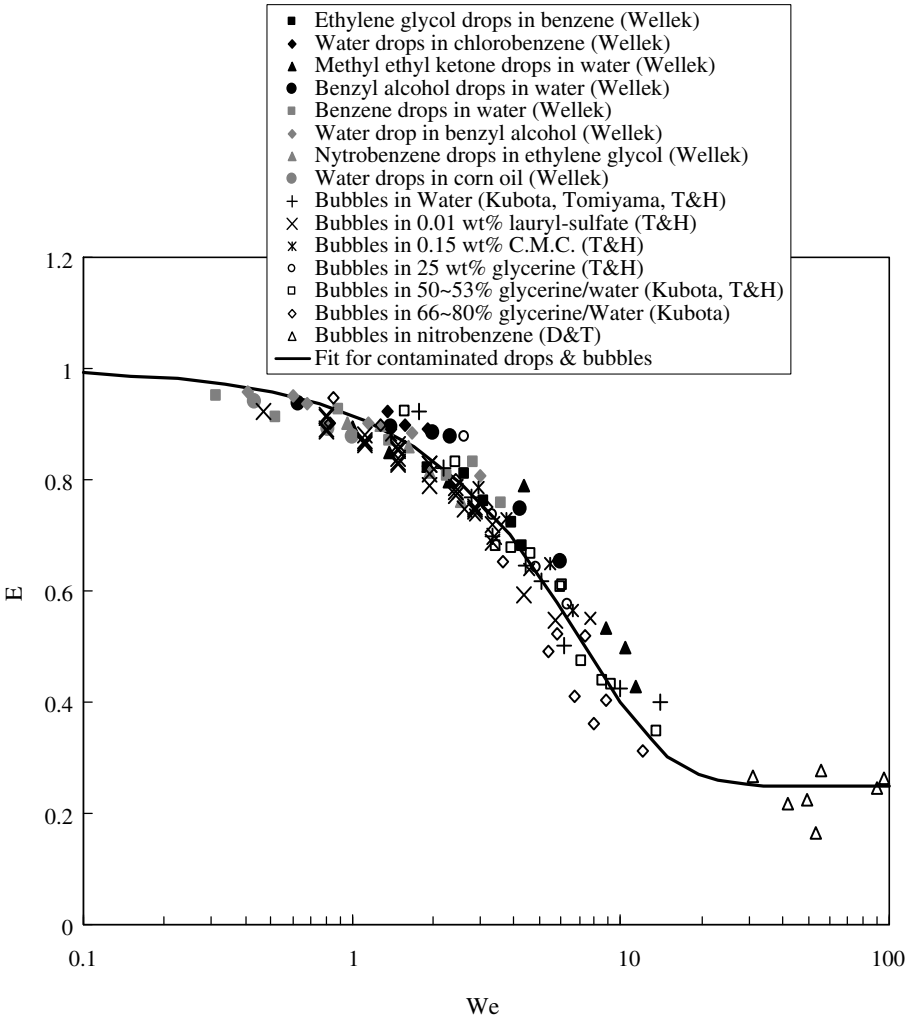

Fig. 18. Aspect ratios of contaminated drops and bubbles in a liquid for $Re_p > 80$ based of data of Davies and Taylor (1950), Welleck et al. (1966), Kubota et al. (1967), Tsuge and Hibino (1977), and Tomiyama et al. (2002).

tions are obtained for both contaminated bubbles and contaminated drops. However, the density ratio effect differentiates these two classes of contaminated fluid particles from each other. For contaminated bubbles ($\rho^* ll 1$), the trends are shown in Fig. 19 with an empirical fit given by

$$\Delta C_D^* \approx \tanh\left[0.0038(WeRe_p^{0.2})^{1.6}\right] \quad (46)$$

However, the correlation of the data and this fit in this figure is not always strong and is effectively qualitative for intermediate deformations.

In contrast to the other fluid particle cases, the *We* influence on ΔC_D^* for contaminated drops in a liquid is well correlated but quite complex in form (Fig. 20). This peculiar dependence was also observed by Hu and Kintner (1955) who suggested that changes in the trend curvature may be related to the onset of trajectory oscillations and irregular (e.g. asymmetric) shapes. While Hu and Kitner recommend an empirical fit for terminal velocity conditions as a function of *We* and Mo, no empirical fit is proposed herein due to the convoluted trends (though Eq. (46) can be used for a qualitative trend). The predictions of contaminated fluid bubbles are summarized in Fig. 21, where the empirical representations are reasonably robust for small Reynolds numbers but are more qualitative for larger Reynolds numbers with intermediate deformation.

8. Aspect ratios and drag for pure drops in liquids

The final fluid particle condition examined for isolated drag behavior is that of pure drops in liquids. Clift et al. (1978) suggested that the aspect ratio for such particles may be related to μ^* and Bo. However, when data is considered in terms of Weber number as in Fig. 22, no substantial dependence on viscosity ratio is observed for $0.8 < \mu^* < 2.4$. When compared to other fluid particle cases, the aspect ratio trends for pure drops in a liquid ($\mu^* \sim 1$) are similar to those for contaminated conditions ($\mu^* \ll 1$) at low *We* but tend to those for clean bubble conditions ($\mu^* \gg 1$) at high *We*. This result may be due to increased sensitivity of even small amounts of surfactants which result for very small particles in conjunction with the reduced amount of recirculation possible when μ^* is order unity. In contrast, large drops with increased Weber num-

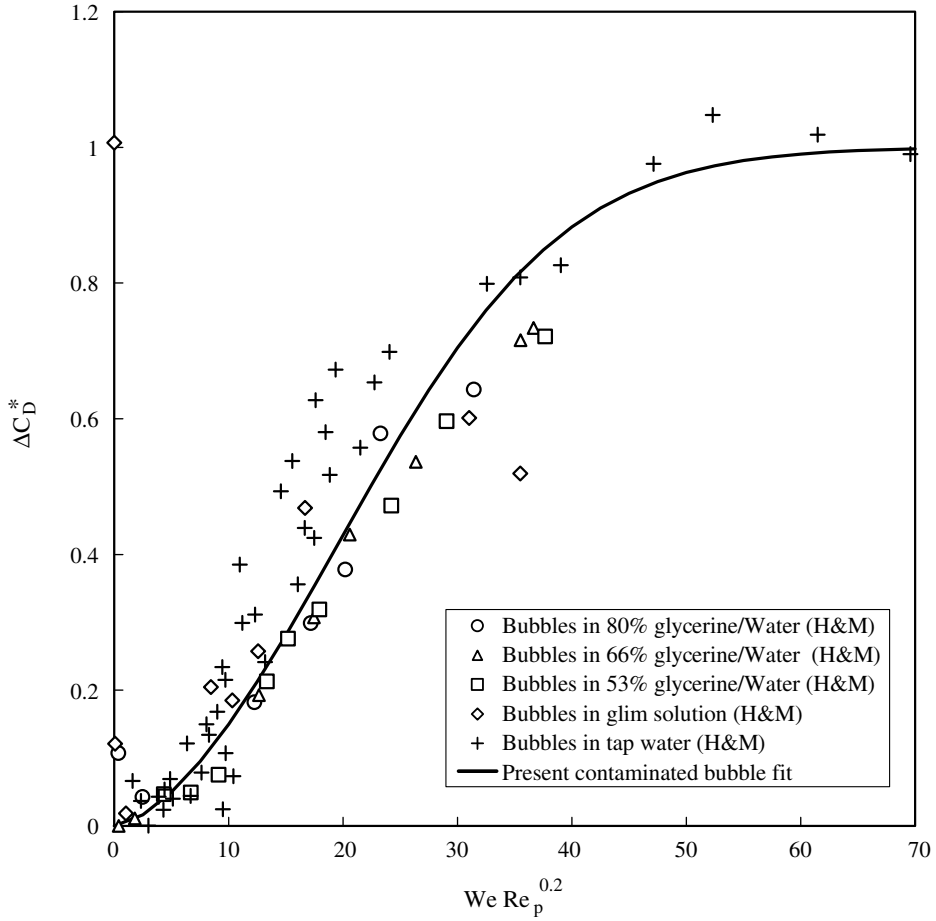

Fig. 19. Incremental drag coefficient ratio for contaminated bubbles in liquids based on data of Haberman and Morton (1953).

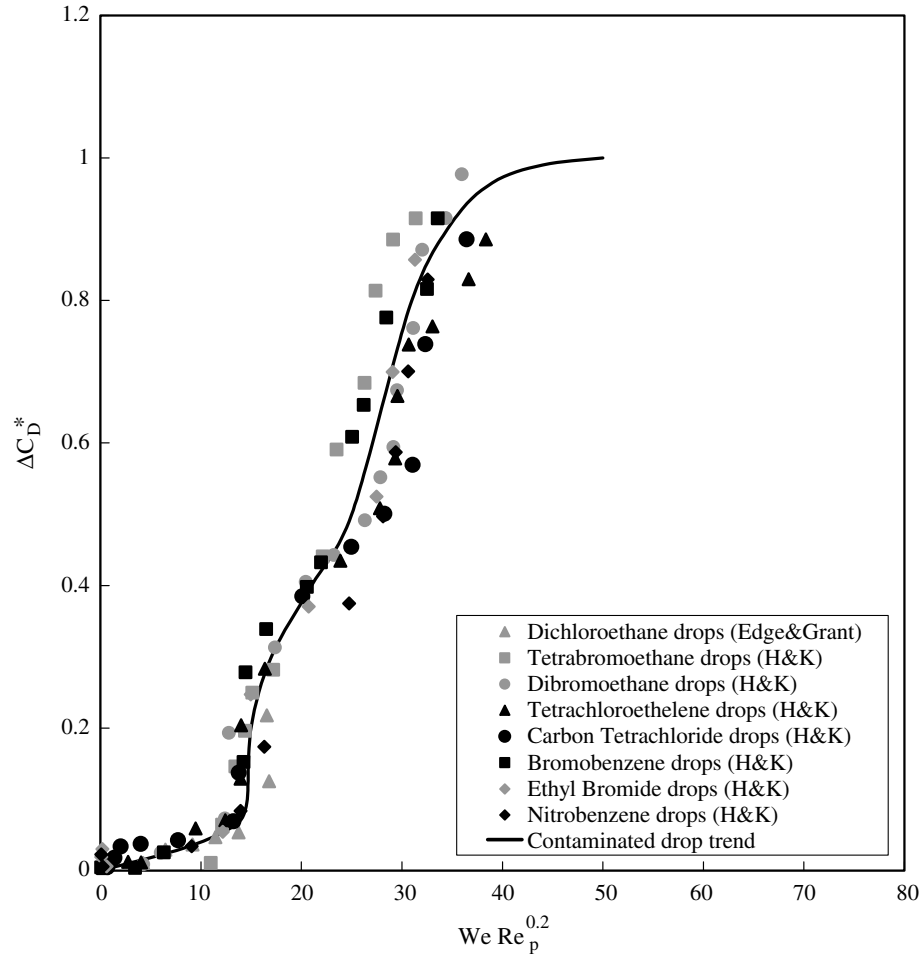

Fig. 20. Incremental drag coefficient ratio for contaminated drops in water based on data of Hu and Kintner (1955) and Edge and Grant (1972).

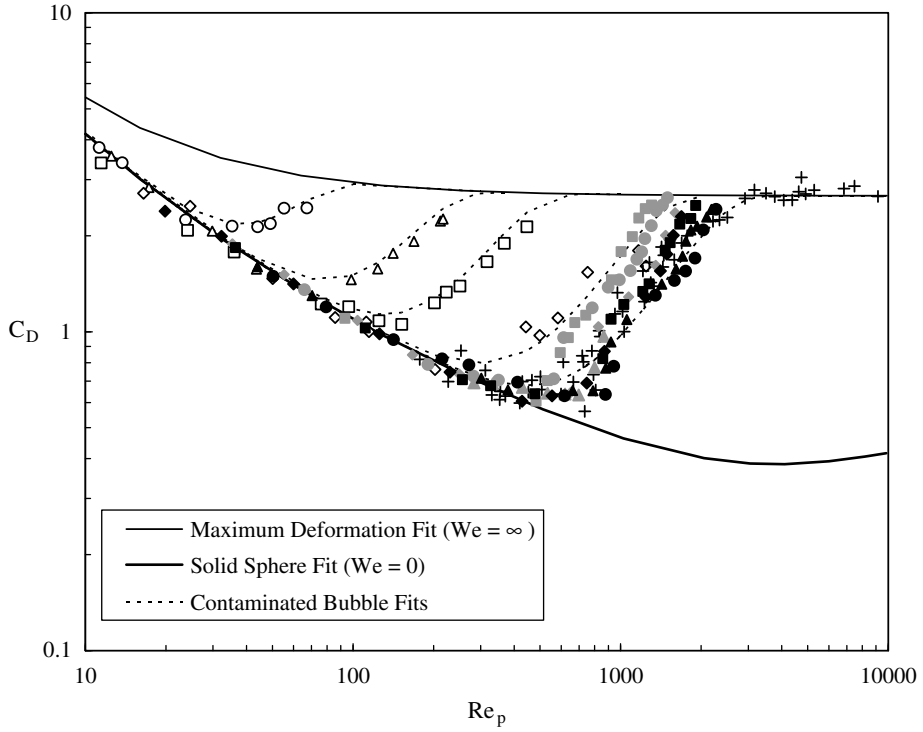

Fig. 21. Drag measurements and predictions for contaminated bubbles and drops in liquids.(data symbols given in Figs. 16 and 17).

ber are much less susceptible to contamination so that they can tend to clean bubble deformations. This issue is further complicated by the fact that significant secondary motion can occur for immiscible drops at these conditions. As such, the behavior for $\mu^* \sim 1$ is not well understood and only a crude approximation to aspect ratio can be put forth for $We < 4$:

$$E \sim 1 - 0.75\tanh(0.07We + 0.001We^4) \quad (47)$$

The normalized drag increment for pure drops in liquids is shown as a function of We in Fig. 23, where the lower-bound C_D is that for a sphere of variable viscosity (Eq. (12)) and the upper bound is that for a maximum-deformation fluid particle (Eq. (36)). The results indicate consider-

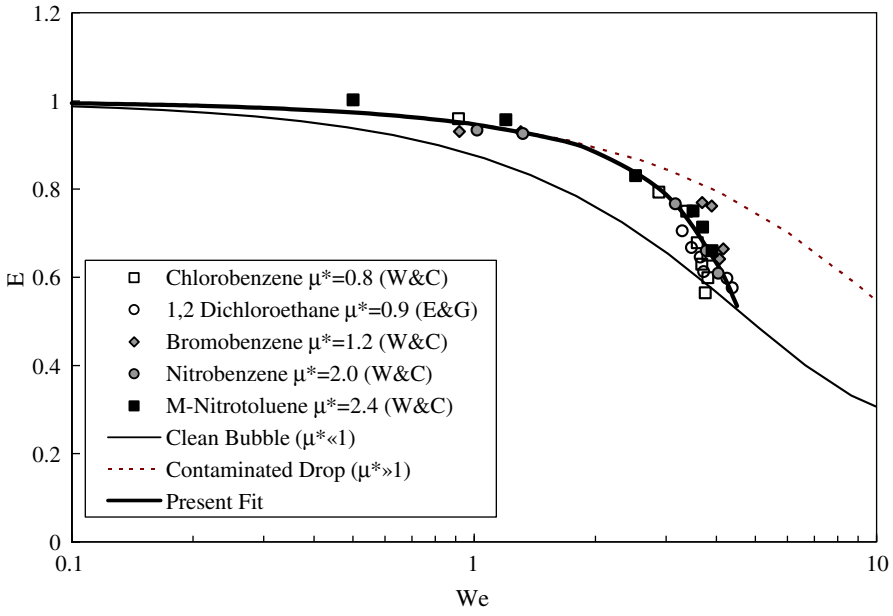

Fig. 22. Aspect ratio of pure drops in liquids with various viscosity ratios (Winnikow and Chao, 1966; Edge and Grant, 1972) compared to contaminated drop and clean bubble fits.

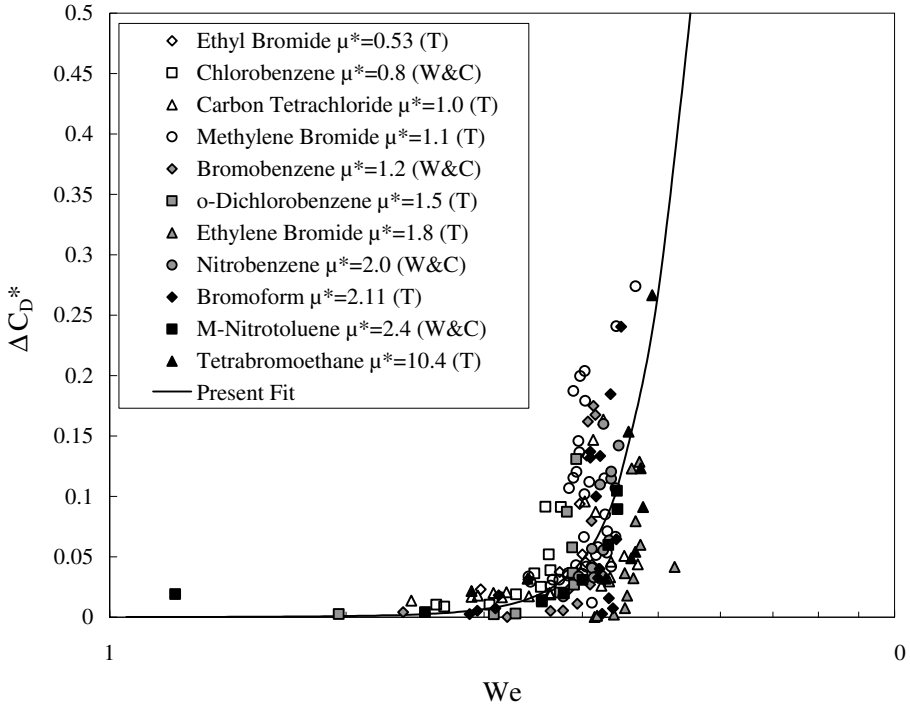

Fig. 23. Incremental drag coefficient of pure drops with various viscosity ratios (Winnikow and Chao, 1966; Thorsen et al., 1968).

able scatter, again without a strong correlation to μ^*. The normalized drag increment for pure drops in a liquid ($\mu^* \sim 1$) approximately follows the fit

$$\Delta C_{D*} \approx 0.5\{1 + \tanh(We - 5.5)\} \quad (48)$$

Because of the large amount of scatter, this expression is only be reasonable for Weber numbers of 4 or less.

9. Conclusions

In summary, fluid particles exhibit deformations and drags which depend strongly on Reynolds number and Weber number consistent with theoretical results. Experimental data and resolved-surface simulations agree well with available theoretical predictions (Taylor and Acrivos, 1964; Moore, 1963, 1965; and Davies and Taylor, 1950) in their respective applicable conditions. The above results also agree reasonably well with the correlations developed herein, which may be helpful to simulate the dynamics of multiphase flow in non-equilibrium conditions.

The shapes considered in this study were limited to those with Weber numbers less than 100, excluding skirted bubbles. For intermediate Reynolds number and separated flow conditions, the aspect ratio data collapsed remarkably well with Weber number especially for clean bubbles and drops in gas. For contaminated bubbles and drops in liquids, the effect of viscosity ratio and surfactant concentration can yield some variations, but again shapes are well correlated with Weber number. In all cases, it was found that there is negligible deformation for particle Reynolds numbers much less than unity, regardless of the Weber number.

The maximum drag for all types of fluid particles was described reasonably well by the simple Darton and Harrison (1974) expression, while a single closed-form expression was obtained for minimum drag (the spherical condition) as a function of viscosity ratio and Reynolds number. The drag for intermediate deformations was found to correlate well with Weber number for clean bubbles, and with the parameter $WeRe_p^{0.2}$ for separated flow conditions ($Re_p > 100$). This led to simple correlations for the incremental drag for bubbles in liquids and drops in gasses. However, the drag increments for contaminated drops in liquids are more qualitative, which may be related to complex interactions which can occur between deformation, surfactant concentration, particle wakes, and trajectory unsteadiness.

Finally, it should be noted that these results and predictions are limited to steady uniform flows and isolated particles. While there are several results available for finite particle concentrations (variations in mass and volume fractions) and wall effects in the literature, additional experimental and numerical data are needed to integrate these effects over a wide range of density ratios, viscosity ratios, Weber and Reynolds numbers, etc. In this regard, recent advances in treating deformable particle may be helpful in further quantifying these trends.

Acknowledgement

The author would like to thank Mr. Chung Wang for creating several of the figures as well as assisting in the data collection and analysis. The work was supported, in part, by a grant from the National Science Foundation.

References

Beard, K.V., 1976. Terminal velocity and shape of cloud and precipitation drops aloft. J. Atm. Sci. 3, 851–864.

Beard, K.V., Prupacher, H.R., 1969. A determination of the terminal velocity and drag of small water drops by means of a wind tunnel. J. Atm. Sci. 26, 1066–1071.

Bel Fdhila, R., Duineveld, P.C., 1996. Effect of surfactant on the rise of a spherical bubble at high Reynolds and Peclet numbers. Phys. Fluid 8 (2), 310–321.

Bhaga, D., Weber, M.E., 1981. Bubbles in viscous liquids: shapes, wakes and velocities. J. Fluid Mech. 105, 61–85.

Blanco, A., Magnaudet, J., 1995. The structure of the axisymmetric high Reynolds number flow around an ellipsoidal bubble of fixed shape. Phys. Fluid 7 (6), 3186–3188.

Bonometti, T., Magnaudet, J., 2006. Transition from spherical cap to toroidal bubbles. Phys. Fluid 18, 052102.

Brenner, H., Cox, R.G., 1963. The resistance to a particle of arbitrary shape in translational motion at small Reynolds numbers. J. Fluid Mech. 17, 561–595.

Clift, R., Gauvin W.H., 1970. The motion of particles in turbulent gas streams. In: Proceedings of the CHEMECA'70, vol. 1, Butterworth, Melbourne, pp. 14–28.

Clift, R., Grace, J.R., Weber, M.E., 1978. Bubbles, Drops and Particles. Academic Press, New York.

Darton, R.C., Harrison, D., 1974. The rise of single gas bubbles in liquid fluidized beds. Trans. Inst. Chem. Eng. 52, 301–306.

Davies, R., Taylor, G.I., 1950. The mechanics of large bubble rising through extended liquids and though liquids in tubes. Proc. R. Soc. London 200, 375.

Duineveld, P.C., 1995. Rise velocity and shape of bubbles in pure water at high Reynolds number. J. Fluid Mech. 292, 325–332.

Edge, R.M., Grant, C.D., 1972. Motion of drops in water contaminated with a surface-active agent. Chem. Eng. Sci. 27 (9), 1709–1721.

Elghobashi, S., 1994. On predicting particle-laden turbulent flows. Appl. Sci. Res. 52, 309–329.

Fan, L.-S., Tsuchiya, K., 1990. Bubble Wake Dynamics in Liquids and Liquid–Solid Suspension. Butterworth-Heinemann, Boston.

Feng, Z.-G., Michealidis, E.E., 2001. Drag coefficients of viscous spheres at intermediate and high Reynolds numbers. J. Fluid Eng. 123 (12), 841–849.

Grace, J.R., 1973. Shapes and velocities of bubbles rising in infinite liquids. Trans. Inst. Chem. Eng. 51, 116–120.

Grace, J.R., T, Wairegi, Nguyen, T.H., 1976. Shapes and velocities of single drops and bubbles moving freely through immiscible liquids. Trans. Inst. Chem. Eng. 54, 167–173.

Haberman, W.L., Morton, R.K., 1953. Experimental investigation of drag and shape of air bubbles. In: David W. Taylor Model Basin Report, vol. 802.

Haberman, W.L., Morton, R.K., 1954. Experimental study of bubbles moving in liquids. American Society of Civil Engineers – Proceedings Separates, 80, Separate no. 387, p. 25.

Harmathy, T.Z., 1960. Velocity of large drops and bubbles in media of infinite or restricted extent. AIChE J. 6, 281–288.

Hu, S., Kintner, R.C., 1955. The fall of single drops through water. AIChE J. 1, 42.

Ishii, M., Chawla, T.C., 1979. Local Drag Laws in Dispersed Two-Phase Flow. ANL-79-105.

Joseph, D.D., 2006. Rise velocity of a spherical cap bubble. J. Fluid Mech. 488, 213–223.

Koebe, M., Bothe, D., Warnacke, H.-J., 2003. Direct numerical simulation of air bubbles in water glycerol mixtures: shapes and velocity fields In: Proceedings of the 4th ASME-JSME Joint Fluids Engineering Conference, FEDSM2003-45154.

Kojima, E., Akehata, T., Shirai, T., 1968. J. Chem. Eng. Jpn. 1, 45.

Kubota, M., Akehata, T., Shirai, T., 1967. The behavior of single air bubbles in liquids of small viscosity. Kagaku Kogaku 31, 1074.

Lamb, 1945. Hydrodynamics. Dover, New York.

Levich, V.G., 1949. Motion of a bubble at large Reynolds numbers. Zhur. Eksp. i. Teoret. Fiz. 19, 18.

Levich, V.G., 1962. Physico Chemical Hydrodynamics. Prentice Hall.

Magnaudet, J., Eames, I., 2000. The motion of high-Reynolds-number bubbles in inhomogeneous flows. Ann. Rev. Fluid Mech. 32, 659–708.

Mei, R., Klausner, J.F., Lawrence, C.J., 1994. A note on the history force on a spherical bubble at finite Reynolds number. Phys. Fluid 6 (1), 418–420.

Mendelson, H.D., 1967. The prediction of bubble terminal velocities from wave theory. AIChE J. 13, 250–253.

Miyahara, T., Takahashi, T., 1985. Drag coefficient of a single bubble rising through a quiescent liquid. Int. Chem. Eng. 25, 146–148.

Moore, D.W., 1963. The boundary layer on a spherical gas bubble. J. Fluid Mech. 16, 161–176.

Moore, D.W., 1965. The velocity rise of distorted gas bubbles in a liquid of small viscosity. J. Fluid Mech. 23, 749–766.

Pan, F., Acrivos, A., 1968. Shape of a drop or bubble at low Reynolds number. I & EC Fund. 7, 227.

Proudman, I., Pearson, J.R.A., 1957. Expansions at small Reynolds number for the flow past a sphere and a cylinder. J. Fluid Mech. 2, 237–262.

Raymond, F., Rosant, J.-M., 2000. A numerical and experimental study of the terminal velocity and shape of bubbles in viscous liquids. Chem. Eng. Sci. 55, 943–955.

Reinhart, A., 1964. Das Verhalten fallender Topfen. Chem.-Ing.-Tech. 36, 740–746.

Ryskin, G., Leal, L.G., 1984. Numerical simulation of a free-boundary problems in fluid mechanics. Part 3. Bubble deformation in an axisymmetric straining flow. J. Fluid Mech. 148, 37.

Saito, S., 1913. On the shape of the nearly spherical drop which falls through a viscous fluid. Sci. Rep. Tohuku Imp. Univ. Sendai, Jpn. 2, 179.

Schiller, L., Naumann, A.Z., 1933. Über die grundlegenden Berechungen bei der Schwerkraftaufbereitung. Ver. Deut. Ing 77, 318–320.

Simpkins, P.G., Bales, E.L., 1972. Water drop response to sudden accelerations. J. Fluid Mech. 55, 629–639.

Tadaki, T., Maeda, S., 1961. On the shape and velocity of single air. Bubbles rising in various liquids. Kagaku Kogaku 25, 254.

Takagi, S., Matsumoto, Y., 1999. Numerical investigations of the lift force acting on bubbles and particles. In: Proceedings of the 3rd JSME/ASME Joint Fluids Engineering Conference, San Francisco, FEDS99-7848, July.

Takagi, S., Prosperetti, A., Matsumoto, Y., 1994. Drag coefficient of a gas bubble in an axisymmetric shear flow. Phys. Fluid 9, 3186–3188, September.

Taylor, G.I., 1949. The shape and acceleration of a drop in a high-speed air stream. Advisory Council on Scientific Research and Technical Development, Ministry of Supply, AC 10647/Phys. C69.

Taylor, T.D., Acrivos, A., 1964. On the deformation and drag of a falling viscous drop at low Reynolds number. J. Fluid Mech. 18, 466–476.

Theofanous, T.G., Li, G.J., Dinh, T.N., 2004. Aerobreakup in rarefied supersonic gas flows. AMSE J. Fluid Eng. 126, 516–527.

Thorsen, G., Stordalen, R.M., Terjesen, S.G., 1968. On the terminal velocity of circulating and oscillating liquid drops. Chem. Eng. Sci. 23, 413.

Tomiyama, A., 1998. Plenary lecture: struggle with computational bubble dynamics. In: Proceedings of the International Conference on Multiphase Flow. Lyon, France, June.

Tomiyama, A., Celata, G.P., Hosokawa, S., Yoshida, S., 2002. Terminal velocity of single bubbles in surface tension force dominant regime. Int. J. Multiphase Flow 28, 1497–1519.

Tsuge, H., Hibino, S.I., 1977. The onset of oscillatory motion of single gas bubbles rising in various liquids. J. Chem. Eng. Jpn. 10, 66–68.

Wallis, G.B., 1974. The terminal speed of single drops in an infinite medium. Intl. J. Multiphase Flow 1, 491–511.

Welleck, R.M., Agrawal, A.K., Skelland, A.H.P., 1966. Shape of liquid drops moving in liquid media. AIChE J. 12, 854–862.

Winnikow, S., Chao, B.T., 1966. Droplet motion in purified systems. Phys. Fluid 9, 50–61.